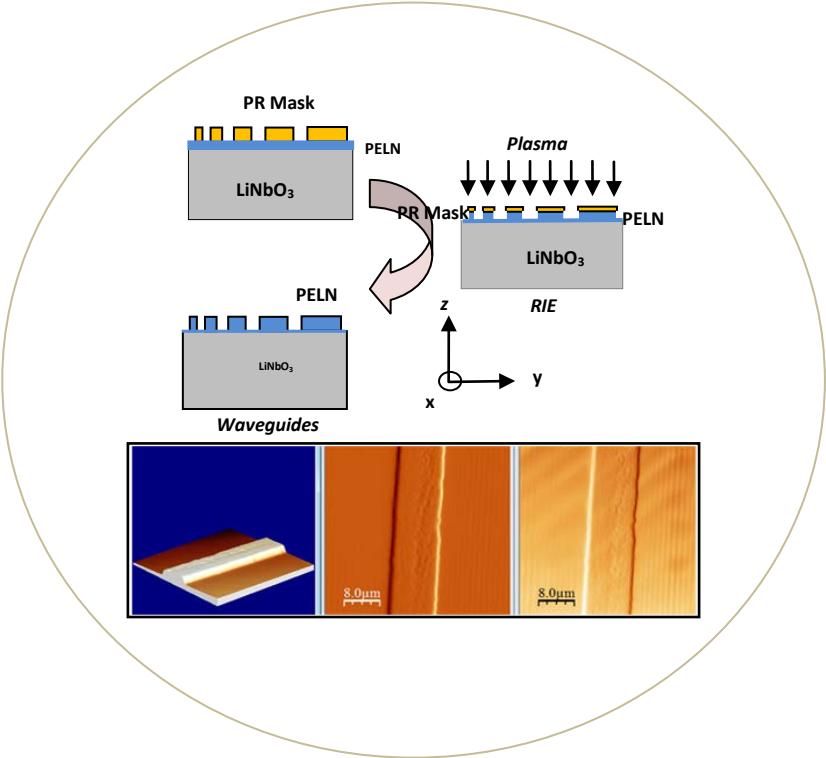# Fabrication of Ridge Waveguides

in Lithium Niobate

ASHRAF MOHAMEDELHASSAN

Master of Science Thesis

Stockholm, Sweden 2012

Royal Institute of Technology

KTH

Fabrication of Ridge Waveguides in Lithium Niobate

Ashraf Mohamedelhassan

Cover photo:

Top: Sample before (upper) and after (right) the etching process and after removing the photoresist

 mask (lower).

Bottom: AFM pictures of tapping mode scanning of C-LN waveguide (Height, amplitude and phase signal respectively).

CONTENTS

ACKNOWLEDGMENT

ABSTRACT

Lithium Niobate (LiNbO$_3$) is an artificial negative uniaxial, non-centrosymmetric, ferroelectric crystal that has a large pyroelectric, piezoelectric, nonlinear and electro-optic coefficients. LiNbO$_3$ is also a widely used material for hosting optical integrated devices.

The main goal of this thesis has been to develop a reliable technological process to fabricate ridge waveguides in LiNbO$_3$ by means of reactive ion etching. Ridge waveguides are particularly promising due to their capability to achieve a strong confinement of light in comparison with traditional (e.g. indiffused) waveguides, yet their fabrication poses several technological challenges.

The main challenge to be faced comes from the fact that LiNbO$_3$ is a hard and relatively inert material, hence relatively difficult to etch. In this master thesis I explored a new technological solution to enhance the etching rate in LiNbO$_3$ which allowed me to develop a dry-etch process to fabricate the ridges with standard photo-resist masks.

Ridge waveguides were made on both –Z and +Z, undoped and MgO-doped congruent LiNbO$_3$ substrates, achieving etching depths of about 500 nm and 300 nm on undoped and MgO-doped materials, respectively. Further characterizations on the ridge profiles were also performed by Atomic Force Microscopy techniques.

وَقُل رَّبِّ زِدْنِي عِلْمًا

1. Introduction

1.1 Background

Optical waveguides are key component allowing confining and guiding light in optical integrated circuits (OIC). Using microstructuring techniques is a basic way to construct devices that deal with controlling and processing light in OIC. The ability to microstructure specific materials is associated to the selectivity in removing or modifying the material over small scales.

Lithium niobate ($LiNbO_3$, LN) is one of the most used materials for hosting OIC devices. $LiNbO_3$ is a synthetic dielectric material that does not exist in nature. Historically it was first discovered in 1949 [1], but the growth as a single crystals was achieved in 1965 [2]. It shows extremely high nonlinear optical coefficients [3], which makes it the favorite candidate for realization of optical devices such as parametric oscillators, parametric amplifiers, second harmonic generators, modulators, etc. Many different techniques have been employed so far for structuring lithium niobate and making optical waveguides in it [4, 5, 6, 7].

This master thesis deals with the development at KTH of suitable microstructuring techniques, (based on photolithography [8] and reactive ion etching [9]) to fabricate ridge waveguides in $LiNbO_3$. The ridge geometry is particularly appealing due to its capability to achieve a strong confinement of the guided light in comparison with other waveguide structures [8].

The main challenge to face in the fabrication of ridge waveguides in lithium niobate comes from the low etching rate of the material and the difficulty to find suitable masks, with high enough selectivity to allow a deep (> 100 nm) etching. The solution I have used in my work was to use proton exchange (PE) to weaken the $LiNbO_3$ surface structure, so to enhance the etching. At same time, the increase in the refractive index associated with the PE process was used to confine the electromagnetic waves within the ridge [10].

Both undoped and MgO-doped congruent lithium niobate substrates were used to fabricate the ridge waveguides. (In this master thesis I shall present the whole fabrica-

1

tion process that I have developed for this purpose at KTH, during my work in the Laser Physics group at the Applied Physics department.)

1.2   **The aim of the thesis**

The aim of this thesis is to fabricate ridge waveguides in $LiNbO_3$, with an as simple as possible fabrication methodology, to achieve high confinement waveguides which could then be further optimised in combination with periodically poled $LiNbO_3$ (PPLN) structures for integrated nonlinear optical devices.

To achieve this main purpose, I used standard microfabrication techniques, in particular photolithography techniques, which are simple, cheap, and give high resolutions over large areas, in combination with reactive ion etching (RIE) techniques I built consist of etched PELN ridges, as shown in Fig.1. below, in which the core guiding region is made of a high refractive index PE layer (n_{PELN}~2.3) embedded on top of the LN substrate (n_{LN}~2.2) and surrounded on both sides and on the top by air (n_{Air} ~1), providing a high refractive –index step, to enhance field confinement.
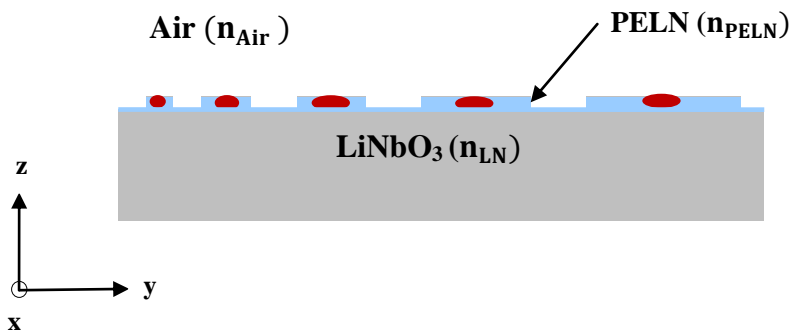
Fig.1.1 Structure of PELN ridge waveguides structures fabricated in this thesis.

1.3 **Outline of Thesis**

This thesis can be divided into two parts:

Part I gives a general introduction on waveguides and LiNbO$_3$. There I shall discuss the fabrication techniques that commonly used to fabricate waveguides in LN, specifically ion beam implantation [5] and two types of ion diffusion, namely Titanium indiffusion [6] and the proton exchange [7]. I shall also provide a description of the proton exchange guiding layer and of the main principle of operation of waveguides, i.e. total internal reflection. Furthermore, I shall introduce the solutions of Maxwell's equations, which describe the electromagnetic field propagation and the modes guided through the confinement layer of waveguides. In chapter 3, I shall provide a brief introduction to lithium niobate (i.e. the growth techniques, crystal structure, etc.) and to undoped and MgO-doped substrates.

Part II is the fabrication part, containing all the details and discussions on the microstructuring techniques that used and developed in my work. It is the core of the thesis work. It contains the details of the proton exchange process, and the conditions used for the ridges. The photolithographic techniques that I used to pattern the ridges are presented in chapter 4, where I give a detailed description of my reactive ion etching studies. To give an idea of what the reactive ion etching actually does, a description of the RIE chamber setup and how to ignite the plasma are also included. I also introduce the basics of the etching mechanisms, in particular the sputtering, chemical etch, and ion-assisted etching, which have to be used synergetically in order to achieve an aniso-tropic etching. This chapter presents also a discussion of the parameters I used to optimize the etching process. The results of the recipe that I used finally chose to etch the ridges are then reported, including a study of their roughness made with the atomic force microscope (AFM) facilities of the Albanova Nanofabrication lab.

At the end of the thesis, in chapter 5, a summary of the work and discussions for further developments are reported.

1.4 **References**

[1]   B.T. Matthias, J. P. Rameika, "Ferroelctricity in the ilmenite structure", Phys. Rev, **76**, 1886 (1949).

[2]   A.A. Ballman,"Growth of piezoelectric and ferroelectric materials by Czochralski technique", J.Am.Ceram.Soc, **48**, 112 (1965).

[3]   R.S. Weis, T.K. Gaylord, "Lithium niobate: summary of physical properties and crystal structure", Applied Phys, **37**, 191(1985).

[4]   F. Laurell, J. Webjörn, G. Arvidsson, J.Holmberg, "Wet etching of proton exchange lithium niobate a novel processing technique", J. Light wave. Technology, **10**, 1606 (1992).

[5]   P.D. Townsend, P.J. Chandler, L. Zhang, "Optical effect of ion implantation", Cambridge University Press (1994).

[6]   W.K. Burns, P.H. Klein, E.J. West, L.E. Plew, "Ti diffusion in Ti:LiNbO$_3$ planar and channel optical waveguides", Appl. Phys, **50**, 6175(1979).

[7]   J.L. Jackel, C.E. Rice, J.J. Veselka,"Proton exchange for high index waveguides in LiNbO$_3$", Appl. Phys. Lett, **41**, 607 (1982).

[8]   H.Nishihara, M.Haruna and T.Suhara, "Optical Integrated Circuits", McGraw-Hill (1989).

[9]   H. Hu, A.P. Milenin, R.B. Wehrspohn, H. Hermann, and Sohler, "Plasma etching of proton exchange lithium niobate", J. Vac. Sci. Technology. A, **24**, 1012 (2006).

[10]   J.L. Jackel, C.E. Rice, J.J. Veselka, "Proton exchange for high index waveguides in LiNbO$_3$", Appl. Phys. Lett, **41**, 607 (1982).

2. Ridge waveguides in LiNbO₃

2.1 Waveguides geometries

The basic picture of a planar (2D) waveguide is shown in Fig.2.1. It consists of a sandwich of three layers called cladding, film, and substrate layer, of refractive indices n_c, n_f, and n_s respectively. The condition to be fulfilled for the light to be confined in the guided layer by total internal reflection is $n_c < n_s < n_f$, with a required thickness value T for the film layer, called the critical thickness [1]. The picture also illustrates the principle of operation of the waveguide, namely total internal reflection: when a ray of light propagating in the high index region (n_f) hits the interface with a medium of a lower refractive index (n_c or n_s) at an angle larger than the critical angle, there is no light that can cross the interface, so that the beam is trapped in the guiding layer.

In the planar waveguide, light confinement takes place only in one direction, as shown in Fig.2.1, where the confinement takes place along z and the propagating along x, but light can still spread out in the perpendicular direction (y-axis) due to diffraction [2].
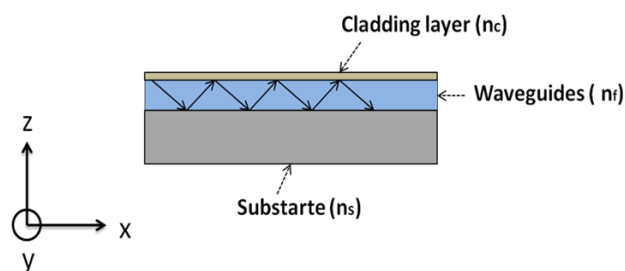
Fig.2.1Planar optical waveguides

To confine light also in the other transverse direction in addition to the depth (z) one needs to create a localized high refractive index region also along y. In this way, by patterning the refractive index profile in 2D (y-z) one can achieve total internal reflection at the upper and lower interfaces as well as at the surrounding interfaces. This

5

corresponds to making a channel waveguide, which avoids light spreading and keeps all the light well confined in both transverse directions.

A channel ridge waveguide structure can be achieved if one by some means succeeds in removing the outer cladding layer film from a planar (2D) waveguide as shown in Fig.2.1, while leaving the waveguide film layer in the central portion intact, with a depth high enough to sustain guidance, as shown in Fig.2.2 (a). In comparison to standard embedded channels made by,e.g. ion exchange (see Fig.2.2 (b)) the ridge structures can allow to a much stronger confinement by achieving a high refractive index step. For instance considering the case of PELN channel waveguides, one could achieve an index step ~0.12 at best in the lateral direction (y in Fig.2.2b), while for the same direction a PELN ridge yields an index increase of ~1.2 (due to the high index step between LN and air).
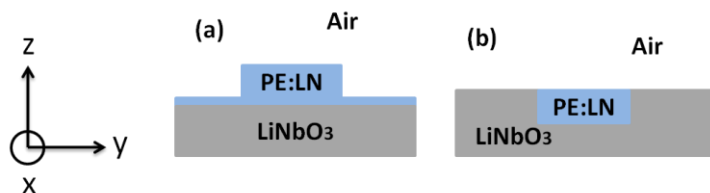
Fig.2.2 (a) Ridge and (b) Buried waveguides structures.

2.2 **Waveguide fabrication techniques**

Many techniques are used to fabricate waveguides in $LiNbO_3$, such as ion/metal diffusion (e.g. titanium indiffusion [3] [4] or the proton exchange [5]) and ion beam implantation [6].

The Titanium indiffusion process consists in depositing a Titanium layer on the surface of a substrate and then thermally indiffusing it into the crystalline substrate by baking at a temperature ~ 1000^oC. This increases the refractive index in the diffusion areas by ~0.001 [3]. Waveguides made by Ti diffusion suffer from increased photore-fractive damage, which means that the devices cannot operate at very high power

densities in the visible [3]. Furthermore, the high processing temperatures complicate the fabrication steps to combine Ti:waveguides with PPLN.

Proton exchange (PE) is one of the most popular methods to fabricate waveguides. It consists in an ion exchange process taking place at the crystal surface, where lithium ions in LiNbO$_3$ are substituted by protons (H$^+$) coming from an acidic melt solution. In contrast with Ti:diffusion, which yields waveguides guiding all polarizations in LN, PE waveguides can only guide light of extraordinary polarization, i.e. light polarized along the crystal optical axis (z, see section 3.5)

Ion beam implantation (IBI) is a process that changes the properties of a material by forcefully embedding in it different types of ions. It typically gives a negative index change in a buried region where the bombarding ions stop in the crystal. IBI is suitable for materials that can have major changes in their properties caused by a small number of implanted particles, typically N$^+$, B$^+$, He$^+$ and Ne$^+$ [7]. IBI has been applied to make waveguides in LiNbO$_3$ [3], but it typically causes damage to the ion-bombarded layer below the surface After the process the samples must be annealed to heal the surface damage [3], but that is not always enough to bring the waveguide losses down to values acceptable for high-quality devices. In addition, it was reported that the ion beam implantation can affect negatively the surface properties, e.g. by increasing the hardness and resistance to oxidation [3].

Another way to fabricate channel waveguides in LiNbO$_3$, is to make ridges by purely chemical (wet) etching, but there are a few drawbacks with that, associated to the isotropic nature of the etch, which results from the fact that the chemical etching works essentially in all directions. HF solutions are typically used to etch LiNbO$_3$ according to the following chemical reaction

$$LiNbO_3 + 9HF \rightarrow LiHF_2 + H_2NbF_7 + 3H_2O$$

It has been reported that, the chemical reaction has fast etching rate along –Z axis than the +Z one [8] [9], this is due to the spontaneous polarization of the ferroelectric substrate, which can make the reactions work at different speeds on the two Z faces, due to the embedded electric field at the surfaces which can either enhance or work against the protonization process. What happens actually in the wet chemical process is that the hydrogen ions in the acidic solution react with oxygen ions at the crystal surface forming

water, and then the fluorine and niobium ions get attached and are removed from the crystal. Then a cycled protonization process takes place letting the Li dissolve into the solution. One way to etch the +Z face is to destroy partially the depolarization field, e.g. by using the proton exchange process.
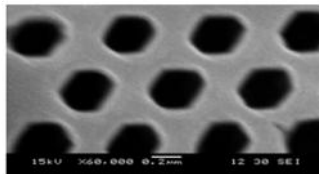
Fig.2.3 ICP plasma etching structure in
LiNbO$_3$ [10].

Nowadays one of the preferred ways to microstructure lithium niobate is to use the dry plasma etching techniques [11] see Fig.2.3 above. This process is a good way to avoid the isotropic processes occurring during chemical wet etching.

In this work, we demonstrate how one can effectively use proton exchange process to significantly enhance the dry etching rates in LiNbO$_3$and make ridge waveguides with a simple photoresist mask.

The ridges waveguides I fabricated were made from proton exchange layers located on top of the surface of the LiNbO$_3$ substrates forming a high refractive index film. The core guiding and confinement region was then patterned by etching, and consisted in a PELN core surrounded by air in the upper layer and on the sides, and having the lithium niobate substrate at the lower interface. The etching structures I made are of the type described by Fig.2.2(b) (rib-waveguides), where the PE layer is not etched all the way through, yet the ridges are high enough to still guarantee the bi-dimensional confinement of light in the transverse plane.

2.3 **Waveguides**

Waveguides can confine and guide the light by a series of total internal reflections. To explain this, suppose that we have a high refractive index region (PELN) working as waveguide layer, lying over a LiNbO$_3$ substrate, and surrounded by air which working as the cladding layer. According to Snell's law, any incident ray of light that forms an angle θ with the normal to the interface can be trapped in the PELN layer

8

through a series of total internal reflections (TIR), when Θ is higher than the critical angles for TIR at the upper (Θ_f) and lower (Θ_s) interfaces, which amount to:

$$\theta_f = \sin^{-1} \frac{n_{(Air)}}{n_{(PELN)}} \qquad\qquad 2.1$$

$$\theta_s = \sin^{-1} \frac{n_{(LN)}}{n_{(PELN)}} \qquad\qquad 2.2$$

Since $n_{(LN)} > n_{(Air)}$, then $\Theta_f < \Theta_s$. This implies three possible ranges for the angle θ, which correspond to cases where light undergoes TIR or escapes from the interfaces as shown in Figs. 2.5, 2.6, and 2.7.

1. $\Theta < \Theta_f < \Theta_s$:

In this case, light undergoes a series of reflections in the guiding layer, but it is able to escape from the upper and lower interfaces, as shown in Fig.2.4. Light is therefore not guided.
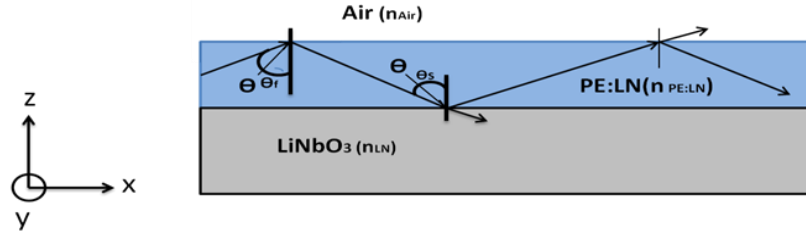
Fig.2.4 No TIR on either the top nor the bottom interfaces = light leaks out from the PELN layer.

2. $\Theta_f < \Theta < \Theta_s$:

The light in this second case is undergoes total internal reflection at the upper interface but will be able to escape from the guiding layer through the substrate according to Snell's law since $\theta < \theta_s$ as shown in Fig.2.5.

9
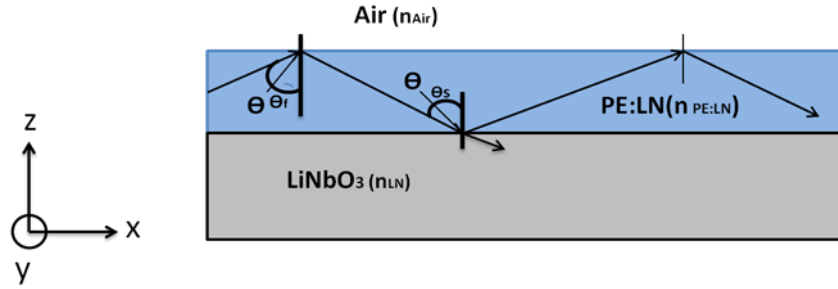
Fig.2.5 Total internal reflection at the top of the PELN layer with radiation escaping at lower interface.

3. $\Theta_s < \Theta < \frac{\pi}{2}$:

This third case corresponds to guidance. As shown in Fig. 2.6 the is light confined in the guiding layer, as it undergoes total internal reflections at both the upper and the lower interfaces and propagates in a zigzag path along x.
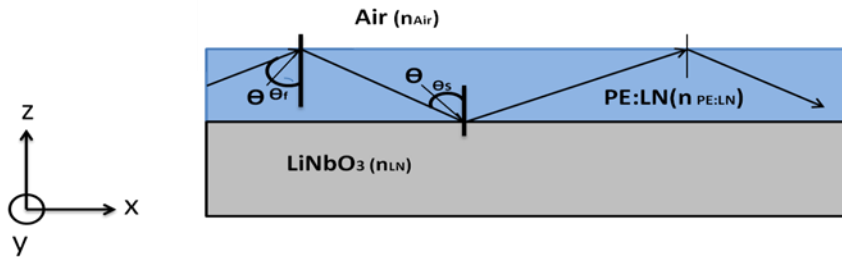
Fig.2.6 Total internal reflection at both top and bottom interfaces corresponds to guidance inside the PELN layer.

The condition to confine light in the PELN layer is then

$$\theta_s < \theta < \frac{\pi}{2} \qquad\qquad 2.3$$

By multiply the sin function to 2.3 we get:

$$\sin \theta_s < \sin \theta < \sin\frac{\pi}{2} \qquad\qquad 2.4$$

Using the equation 2.2, this gives

$$\frac{n_{(LN)}}{n_{(PELN)}} < \quad sin\,\theta \quad < 1 \qquad\qquad 2.5$$

$$n_{(LN)} < n_{(PELN)} sin\,\theta < n_{(PELN)} \qquad\qquad 2.6$$

The value $n_{eff} = n_{(PELN)} sin\,\theta$ is called the effective index of the guided mode. In the more general case of a graded index waveguide, the effective indices of its guided modes can be calculated, for a given refractive index distribution $n = n\,(z)$, as the solutions of an eigenvalue equations (see ref. [1] for more details). So far, we have considered planar waveguides. In a ridge waveguide, light is confined also in the other transverse direction, i.e. y (if we were to follow the notation of in Fig. 2.7, where x is the propagation direction in the waveguide).

To calculate the effective indices n_{eff} of the guided modes in a ridge waveguide, one can use the simplified treatment of effective index theory [1], an analytical method applicable to waveguide with 2D confinement. The waveguide is decomposed into three regions (RI, RII and RI), which are treated as three asymmetric planar waveguides, in the x direction, having three different effective indices, n_{eff} (RI), n_{eff} (RII), and n_{eff} (RI) see Fig.2.7 (a) below.
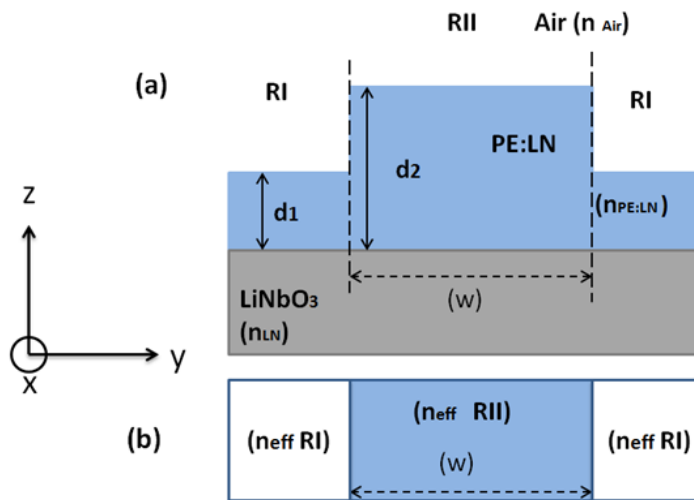
Fig.2.7 The effective index method applied to ridge waveguides.

The guided modes can be determined by finding the effective index vertically for the regions (RI) and (RII) see Fig.2.7 (a), which they have PELN layers thicknesses (d1) and (d2) respectively. Then the ridge waveguides effective index (n_{eff}) can be calculated by solving horizontally the eigenvalue problem for a simple symmetric planar waveguides lied along y direction, see Fig.2.7. (b), having a cover layer with n_{eff} (RI), waveguides layer with thickness (w) an effective index n_{eff} (RII), and substrate with effective index n_{eff} (RI).

2.4 **Prism coupled method**

The reduced thickness of thin film waveguides requires specific techniques for light coupling. The prism coupler is a way to couple the light into the waveguides, illustrated in Fig. 2.8. Light can be coupled into a planar waveguide via a high-refractive index prism attached on its surface. θ is the incidence angle of light from the prism into the waveguides, γ is the prism base angle and alpha is the external incidence angle into the prism. d is the thickness of the waveguides layer (PELN).
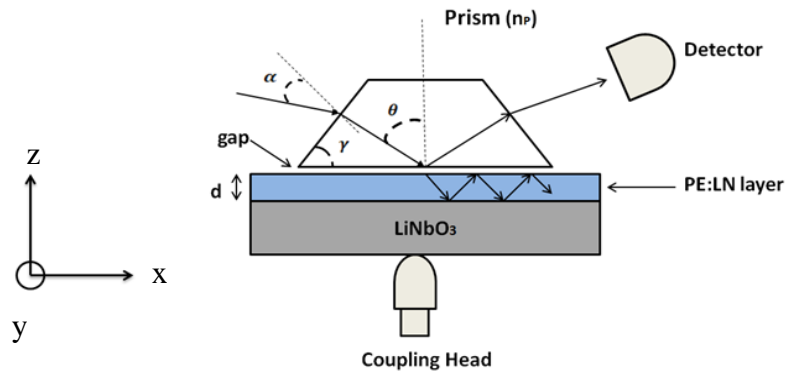
Fig.2.8 Sketch illustrating prism coupling on a PELN planar waveguide.

The light beam that goes into the prism will undergo total internal reflection at the prism base, unless the prism and waveguide are brought into such a close contact that tunneling across the intermediate air layer can occur. Then the waves in the prism and in the waveguide can be coupled through their evanescent fields when the projection along the waveguide axis of the propagation wave vector of light in the prism equals the propagation vector of a guided mode in the PELN layer.

2.5 **Guided modes descriptions**

Ridge PELN waveguides allows us to guides the transverse electric (TE) mode in the x and y-cut substrates while the transverse magnetic (TM) mode in the z-cut substrate only (Which gives a property to the access to control the polarization in optical devices).

In this work, the ridges were fabricated along x, as a propagation direction, thus transverse magnetic field polarized along y-axis and electric field mainly polarized along z-axis this and due to the PE only light of extraordinary polarization allow to be guided in ridges PELN waveguides using z-cut substrate.

The equations describing propagating of an electromagnetic harmonic wave at frequency ω propagating along the x-axis direction of a planar PELN waveguide as in Fig.2.6, assuming lossless (zero conductivity), and non-magnetic materials (permeability $\mu=\mu_o$) can be written in the form:

$$E(x, z, t) = E(y, z) \exp i(\omega t - \beta x) \tag{2.9}$$

$$H(x, z, t) = H(y, z) \exp i(\omega t - \beta x) \tag{2.10}$$

Where E and H are the electric and magnetic fields respectively, β is the mode propagation constant, ω the angular frequency$= 2\pi c/\lambda$, c is the light velocity in vacuum $= 1/\sqrt{\varepsilon_0\mu_0}$, and ε_0 and μ_0 are the dielectric permittivity and magnetic permeability of free space, respectively.

Suppose that the medium is isotropic and linear ($D = \varepsilon E$). Then by using the Maxwell's curl equations below we have:

$$\nabla \times E = -\mu_0 \frac{\partial H}{\partial t} \tag{2.11}$$

$$\nabla \times H = \varepsilon_0 n^2 \frac{\partial E}{\partial t} \tag{2.12}$$

In a planar waveguide, the electromagnetic field can be classified in two different modes with mutually orthogonal polarization states [1]. One is the TE mode, which consists of the field components H_x, E_z and H_y , and the other is the TM mode, which has the field components E_x, H_z and E_y .

13

This classification depends on whether the components along the propagation direction, E_y or H_y are zero or not.

The TE mode, has $E_y = 0$ and $H_y \neq 0$. The wave equation is then given by:

$$\frac{\partial^2 E_x}{\partial y^2} + (n^2 k_0^2 - \beta^2) E_x = 0 \qquad\qquad 2.13$$

where $k_0 = \frac{2\pi}{\lambda}$, and λ is the wavelength at free space. The magnetic components for the TE mode are given by:

$$H_y = -\frac{\beta}{\omega\mu_0} E_x \qquad\qquad 2.14$$

$$H_z = -\frac{1}{j\omega\mu_0} \frac{\partial E_x}{\partial y} \qquad\qquad 2.15$$

The other polarization state (TM mode), has $E_y \neq 0$ and $H_y = 0$.

And the mode wave equation can be given by:

$$\frac{\partial^2 H_x}{\partial y^2} + (n^2 k_\circ^2 - \beta^2) H_x = 0 \qquad\qquad 2.16$$

And the electric-field components in this mode are given by:

$$E_y = \frac{\beta}{\omega\mu_0} H_x \qquad\qquad 2.17$$

$$E_z = -\frac{1}{j\omega\epsilon_0\mu_0 n^2} \frac{\partial H_x}{\partial y} \qquad\qquad 2.18$$

14

2.6 **References**

[1] H.Nishihara, M.Haruna and T.Suhara, "Optical Integrated Circuits", McGraw-Hill (1989).

[2] G. Lifante," Intergraded photonics fundamentals", John Wiley and sons Ltd, (2003).

[3] W.K. Burns, P.H. Klein, E.J. West, L.E. Plew, "Ti diffusion in Ti:LiNbO$_3$ planar and channel optical waveguides", Appl. Phys, **50**, 6175 (1979).

[4] W. S. Yang, H.-Y. Lee, W.K. Kim, D.H.Yoon, "Asymmetry ridge structure fabrication and reactive ion etching of LiNbO3", Optical materials, **27**, 1642 (2005).

[5] J.L. Jackel, C.E. Rice, J.J. Veselka,"Proton exchange for high index waveguides in LiNbO$_3$", Appl. Phys. Lett, **41**, 607 (1982).

[6] P.D. Townsend, P.J. Chandler, L. Zhang, "Optical effect of ion implantation", Cambridge University Press (1994).

[7] Yu.N. Korkishko and V.A. Fedorov, "Ion exchange in single crystals for Integrated optics and optoelectronics", Cambridge international science Publishing (1999).

[8] F. Laurell, J. Webjörn, G. Arvidsson, J.Holmberg, " Wet etching of proton exchange Lithium niobate a novel processing technique", J. Light wave.Technology, **10**, 1606 (1992).

[9] H.Hu, R. Ricken, W. Sohler, and R.B. Wehrspohn, "Lithium niobate ridge waveguides fabricated by wet etching", IEEE PHOTON TECHN LETT, **19**, 6 (2007).

[10] H. Hu, R. Ricken and W. Sohler, " Etching of Lithium niobate: form ridge waveguides to photonic crystal structures", Eindhoven, The Netherlands (2008).

[11] H.Hu, A.P. Milenin, R.B. Wehrspohn, H. Hermann, and Sohler, "Plasma etching of proton exchange lithium niobate", J. Vac. Sci. Technol. A, **24**, 1012 (2006).

3. Lithium niobate

3.1 Introduction

Lithium Niobate (LiNbO$_3$, LN), is an artificial, negative, uniaxial, non-centrosymmetric, ferroelectric crystal. For its manifold properties, LiNbO$_3$ is a widely used crystal in different fields of science and technology. As matter of fact, LiNbO$_3$ is characterised by large pyroelectric, piezoelectric, nonlinear and electro-optic coefficients and it is also employed for applications in which acoustic and acousto-optic properties are required.

3.2 Crystal growth

LiNbO$_3$ does not exist in nature. The preferred method to growth this crystal is the Czochralski technique. Fig.3.1(a) shows the typical setup employed in this method. LiNbO$_3$ is grown from pure powders of lithium carbonate (Li$_2$CO$_3$) and niobium pentoxide (Nb$_2$O$_5$) that are melted in a platinum crucible. The following chemical reaction regulates the crystal growth:

$$Li_2\,CO_3 + Nb_2O_5 \rightarrow 2LiNbO_3 + CO_2$$
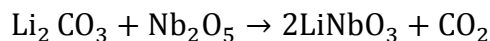
The reaction occurs in the platinum crucible that is placed inside a furnace. The reactants are heated to the melting point, and then they kept in the liquid phase. Then a seed attached to the end of a pull rod is brought close to the melt surface, and heated to a temperature near the melting point of LiNbO$_3$ (1250℃) [1]. After that, the pulling rod is lowered to get into contact with the melt surface, so that the reaction at the solid – liquid interface takes place. At the right temperature, just above the melting point of LiNbO$_3$, atoms from the liquid will adhere to the seed. At higher temperatures, the seed melts while on the contrary at lower temperatures the melt freezes locally around the seed. During the growth of the crystal, the rod is kept in rotation in order to guarantee homogeneity and to avoid thermal gradients in the crystal.

16

a)   b)
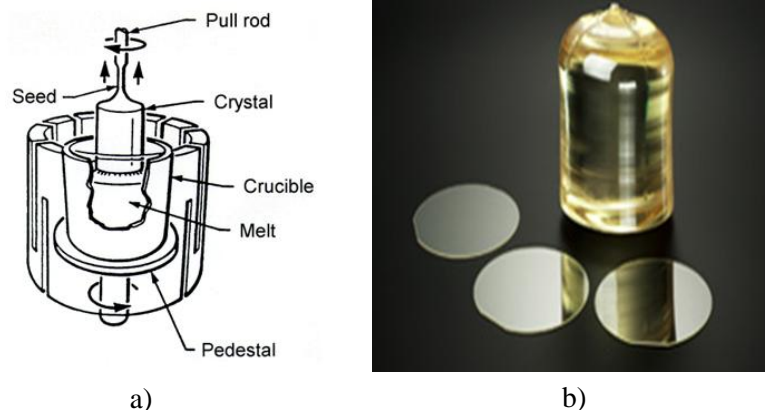
Fig.3.1 a) Setup view for the growth by using the Czochralski technique [2], b) Single crystal of LiNbO$_3$ [3].

The diameter of the crystal boule is kept constant during the growth until the desired length is reached. The control of boule dimensions is achieved by setting the choosing the diameter of the crucible, the rotation and the pulling rate. The crystal is finally separate from the melt by increasing the temperature and raising the rod. After the separation, the growth chamber is cooled down to room temperature. The crystal is then cut and polished.

LiNbO$_3$ can be grown in a wide range of compositions. The composition exactly matching the chemical compound LiNbO$_3$, having a ratio of [Li]:[Nb]:[O] of 1:1:3 is commonly referred as Stoichiometric Lithium Niobate (SLN). However, due to the volatility of the Li ions and their consequent deficiency in the crystal, the growth of the stoichiometric composition is quite challenging. The composition that is easiest to grow with a good uniformity (and is therefore commonly used) is the congruent one (C-LiNbO$_3$).

Historically, LiNbO$_3$ has been prepared in both stoichiometric and congruent composition. The latter is now the preferred one because of its highest optical quality and uniformity. Fig.3.2 shows the phase diagram for LiNbO$_3$. There is a unique point called congruent point, at which both the solid and the liquid phase can co-exist and it corresponds to the highest point on the melting temperature line. The ratio of Li to the total Li and Nb concentration is 48, 45% [4] and it has the same molar ratio in the solid and in the melt crystal. This feature makes it easier to growth this composition with good

homogeneity. Crystals grown in other points of the phase diagram have in general much greater variation in composition, showing inconsistencies in refractive indices [4].
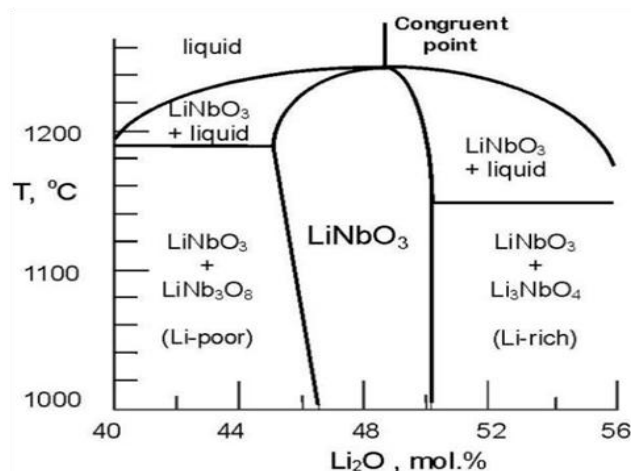
Fig.3.2 Li_2O- Nb_2O_5 equilibrium temperature –composition phase diagram of $LiNbO_3$ [5].

MgO-$LiNbO_3$ is grown from a melt with Li/Nb ratio equal to that of an undoped congruent melt with addition of 5 mol% of MgO [6]. MgO, with 5mol% concentration, has been shown to be a good dopant to improve the resistance to photorefractive damage and to preserve the large non linear optical coefficient so to make it capable to work at substantially higher powers [7], moreover it has stable refractive index.

3.3 $LiNbO_3$ crystal structure

$LiNbO_3$ belongs to the perovskite crystal family. The crystal structure consists of planar sheets of oxygen atoms in a distorted hexagonal close-packed configuration [8] showed in Fig.3.3. The interstices of the oxygen octahedra are filled one-third by lithium ions, one-third by niobium and one-third is vacant. In the z direction, the atoms are placed in the interstices in the following order: Nb, vacancy, Li [9].

The $LiNbO_3$ crystal below the Curie temperature, i.e. in its ferroelectric phase, exhibits three-fold rotation symmetry about the c-axis, so $LiNbO_3$ is a trigonal crystal.
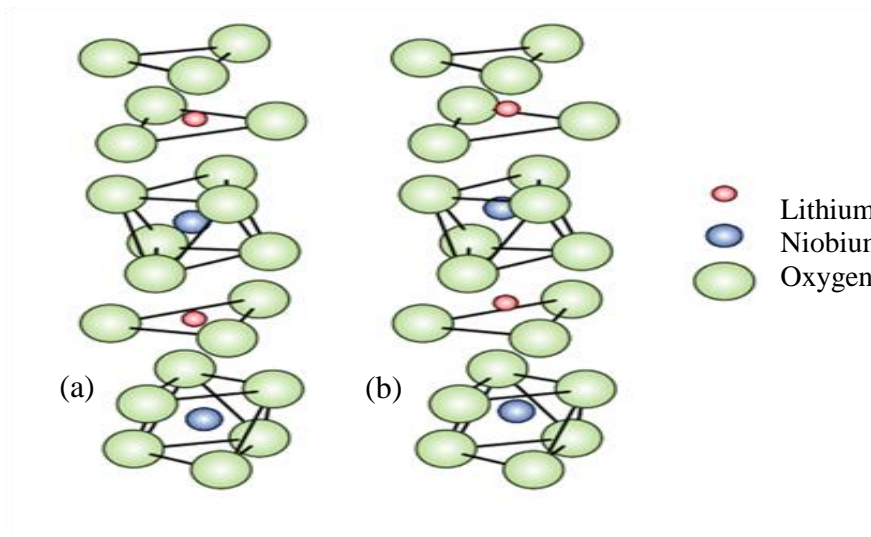
Fig.3.3 Paraelectric (a) and Ferroelectric (b) phase in LN [8].

LiNbO$_3$ is a trigonal crystal since it exhibits three-fold rotation symmetry around the c-axis. It exhibits mirror symmetry of three planes lying 60° apart and forming a threefold rotation axis, as shown in Fig.3.4. These two symmetries classify LiNbO$_3$ as a member of the 3m point group it also belongs to the R3c space group [10].

LiNbO$_3$ is ferroelectric below the Curie temperature (1140 ℃) whereas when above (but below the melting temperature) the displacement of the Li and Nb ions in respect to the oxygen planes vanishes and therefore the spontaneous polarization vanishes too, then the paralectric phase arises.

The orientation of the c-axis is given by the position of two neighbor lithium and niobium atoms, as well as of the vacancies with respect to the closed-packed oxygen planes. The two atoms are displaced slightly away from the octahedra center along c-axis arising a spontaneous polarization aligned along this axis. These pairs can work as individual axis and they can be aligned either up or down indicating the domain polarizations. The standard methods to determine the c-axis orientation is to compress the crystalline in the c-axis direction. The c$^+$ face (the positive end of the ferroelectric dipole) will exhibit a negative charge under compression, when the niobium and the lithium ions move closer to their paraelectric position, thus reducing the dipole, while

19

the c⁻ face (the negative end of the dipole) exhibits a positive charge under compression [4].
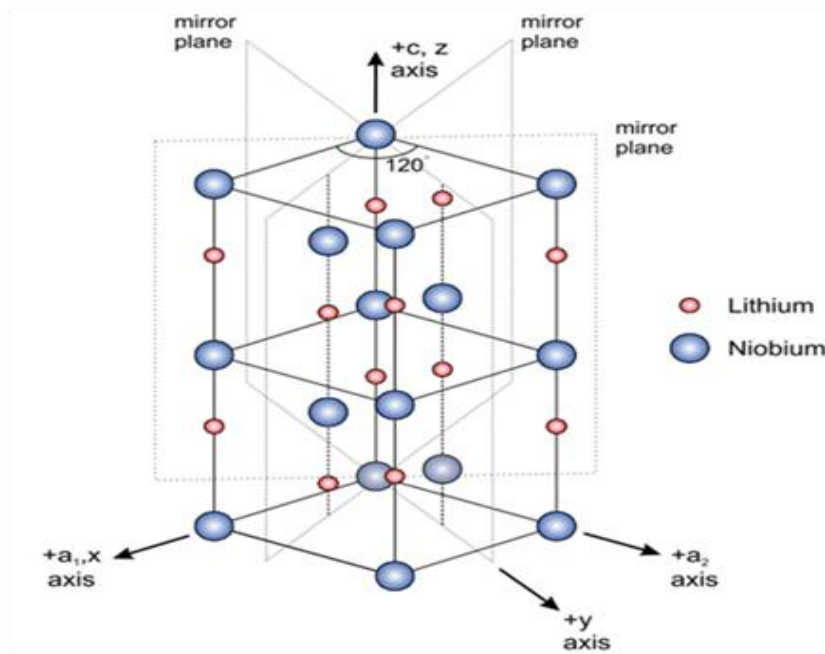
Fig.3.4 LiNbO$_3$ symmetry mirror phase.

There are two different unit cells in LiNbO$_3$: hexagonal or rhombohedra. In the first one, showed in Fig.3.4, the z-axis is chosen to be parallel to the c-axis of the crystal. The y-axis is chosen to be parallel to one of the mirror plane, and the x-axis chosen so to form a right-handed system [11]. This conventional hexagonal unit cell contains six formula weights (147.843 amu). The three equivalents a axis in the conventional hexagonal unit cell are 120 degree apart and lie in a plane normal to the c-axis. These axis are chosen to be perpendicular to the mirror planes (a$_1$and a$_2$ are shown in Fig.3.4). It is conventional to take in this hexagonal unit cell the Nb as the origin, for the congruent compounds LiNbO$_3$ unit cell length a, are a$_H$ = 5.1536 Å. While in the other type rhombohedra unit cell, a$_R$ = 5.474 Å and the angle α between these three axis are 56.180 degree [12]

3.4 Photorefractive effect in $LiNbO_3$

The photorefractive effect is the variation of the refractive index due to optically generated charge carriers. The photorefractive effect in $LiNbO_3$ is caused by charges migrations and accumulation due to the photovoltaic effect. Since, $LiNbO_3$ is electro-optic, the accumulation of charges generate an electric field that locally changes the refractive index. When a crystal of C-$LiNbO_3$ is illuminated by green or blue light ($\lambda <$ ~550 nm) electrons from impurities (Fe^{2+}, Fe^{3+}) are photo-excited and generate a light-induced variation of the refractive index. Photorefraction can manifest itself in various ways like phase modulation, beam break-up, Bragg scattering, reduction of efficiency in nonlinear interactions, beam distortion, etc [12].

To minimize these effects, one can for instance use to work at higher temperature or by making the $LiNbO_3$ more stoichiometric, in order to reduce the presence of impurities which are located in lithium vacancies. Another approach is, as mentioned in 3.2, to add metal impurities such as Magnesium. The optical damage is then lowered preventing the build up of the static field that cause the photorefractive effect [12].

3.5 Optical transmission and refractive indices

The lithium niobate has found widespread optical applications due to its wide transmission range in Fig.3.5 the solid line shows the transmission spectrum for C-$LiNbO_3$, from 350nm to the mid infrared 5μm.
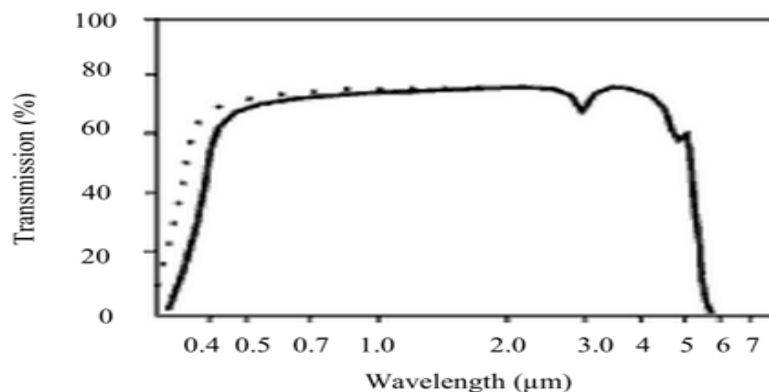
Fig.3.5 Transmission spectrum of C- $LiNbO_3$ solid line [13]

$LiNbO_3$ is a birefringent crystal. In such a material the light propagate in a linear superposition of two orthogonal polarized waves (eigenwaves), in the case of the uniaxi-

al ($n_x = n_y$, n_z) birefringent crystals, these eigen waves are also called ordinary and extraordinary waves.

In z-cut LiNbO$_3$, the optical axis is coincident with the c-axis, and perpendicular to the waveguides layer. The propagation direction of normally incident light is perpendicular to the crystal c-axis.

In the proton exchange waveguides that performed on the z-cut substrate, the substrate layer is associated with permittivity tensor as followed:

$$\varepsilon_s = \epsilon_\circ \begin{bmatrix} n_o^2 & 0 & 0 \\ 0 & n_o^2 & 0 \\ 0 & 0 & n_e^2 \end{bmatrix}$$

where n_o is the ordinary refractive index, which is defined as to being polarized perpendicular to the optical axis of the crystal, and n_e is the extraordinary index, the index polarized perpendicular to the ordinary ray. The ordinary refractive index does not dependent of the beam propagation direction, while the extraordinary is dependent. Compared to the z-cut substrate values above, using the PE technique one can find the value of an extra ordinary refractive index of PELN layer is greater than the LiNbO$_3$ substrate, and vice versa for the ordinary refractive index, which is less than LiNbO$_3$ substrate, in other words, the extra ordinary increased while the ordinary index decreased.

The PE process increases the extraordinary index that lie along the z-axis, and the decreases the ordinary one along x and y-axis. The extraordinary and the ordinary refractive indices of the Lithium niobate crystals well approximated using Sellmeir equation, which gives the relation between the refractive index and the wavelength [14]. The Sellmeir equation can be written as:

$$n^2 = 1 + \frac{A\lambda^2}{\lambda^2 - B} + \frac{C\lambda^2}{\lambda^2 - D} + \frac{E\lambda^2}{\lambda^2 - F}$$

Moreover, by using the coefficients for Sellmeier equation for the LiNbO$_3$ [14], the dispersion curves of the C-LiNbO$_3$ and MgO-LiNbO$_3$ in transparency region as a function of wavelength shown in the Fig.3.6 and Fig.3.7 respectively.
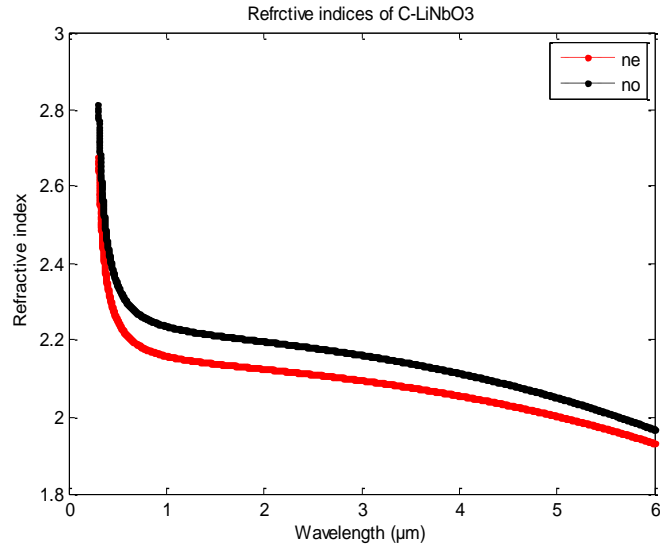
Fig.3.6 Refractive indices of C-LiNbO$_3$ as functions of wavelength.
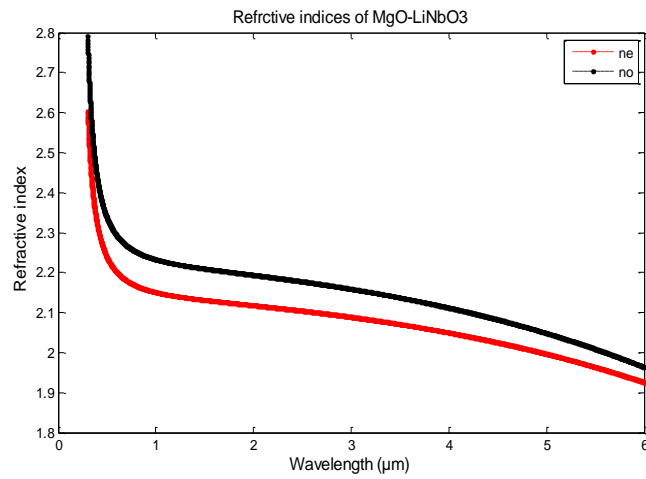
Fig.3.7 Refractive indices of MgO-LiNbO$_3$ as functions of wavelength.

3.6 **References**

[1]   D.H. Jundt and G. Foulon,"Boules of $LiNbO_3$ congruent grown by the Czochralski technique", in properties of Lithium niobate (Ed, K.K. Wong) pp.25-27, INSPEC, London (2002).

[2]   B.Q.Li, "Solidification processing of materials in magnetic fields", JOM- e, **50,** 2 (1998).

[3]   http://www.smm.co.jp/E/business/material/product/lithium/

[4]   EMIS Data review series No.**5**, "Properties of lithium niobate", INSPEC London (1989).

[5]   G Malovichko, V Grachev, E kokanyan and O Schirmer, "Optimization of lithium niobate for advanced applications by variation of extrinsic and intrinsic defect subsystems", Ferroelectrics **258** ,131 (2001).

[6]   D.H. Jundt, M.C.C Kajiyama, D.Djukic, M. Falk, "Optical methods to character-ize crystal composition of MgO doped lithium neonate", Journal of crystal growth **312**, 1109 (2010).

[7]   P. Gunter and J.P.Huignard Ed, "Photorefractive materials and their applications I", Topic in Applied Physics, **61**, (1988).

[8]   R. S. Weis, T.K. Gaylord, "Lithium niobate: summary of physical properties and crystal structure", Applied Phys, **37**, 191(1985).

[9]   S.C. Abrahams, J.M. Reddy, J.L. Bernstein,"FerroelectricLithium niobate III. Single crystal X-ray studies at 24^oC ", J.Chem.Phys. Solids,**27**, 989(1966)

[10]   B. K. Vainshtein, "Symmetry, and Methods of structural Crystallography", Springer series in solid-state science, **15** (1981).

[11]   IRE Standards on Piezoelectric Crystals**,** IEEE Standard **176**; also. Proc. I R E**,** vol. **37,** 1378-1395, December (1949).

[8]   Yu. N.Korkishko and V.A. Fedorov, "Ion exchange in single crystal for integrated optics and optoelectronics", Cambridge international science publishing, England (1999).

[13]   M. Lawrence, "lithium niobate integrated optics", Rep. Prop. Phys, 363 (1993).

[14]   D. Jundt, D.E.Zelmon and D.L small," Infrared corrected Sellmeier coefficients for congruently grown lithium niobate and 5mol% magnesium oxide doped lithium niobate", J. Op. Am. B, vol.**14**, No.12, December (1997).

4. Fabrication of PE:LN waveguides

4.1 Introduction

Lithium niobate is a hard and relatively inert material, hence relatively difficult to etch. Standard micromachining technologies, such as laser ablation or, wet acid etching, are often not suitable for achieving the fine and high-aspect ratio typically required for optical devices. Specifically, the low-etching rates of lithium niobate make high-quality etching already challenging for depth of the order of micrometers. With reactive ion etching (RIE) [1] sub micrometer etching depths have been achieved in LiNbO$_3$ substrates, by using high-density plasma tools, such as inductive coupled plasma (ICP), to enhance the etching rate and Chromium masks to maximize selectivity [2].

In this master thesis, I explored a new technological solution to enhance the etching rate of LiNbO$_3$ in the RIE process using a standard photo-resist mask and I used it to fabricate 500 nm high PE:LN waveguides. This chapter will provide an overview of the whole fabrication process I developed for this purpose, at the Albanova nanofabrication lab at the Applied Physics department.

4.2 The fabrication steps

As discussed in chapter 2, several techniques are available to make waveguides in lithium niobate, such as titanium in-diffusion [3] [4], and proton exchange (PE) [5]. The proton exchange technique is cheap, simple and implies processing at relatively low temperatures (~200ºC). Among all diffusion and exchange techniques, PE is the one that can provide the highest refractive index increase. Indeed, along the crystal optical axis, i.e. the extraordinary one, the refractive index is increased of ~0.12 at 633 nm [6]. Hence tha latter allows the strongest confinement of optical fields in a guiding structure. For comparison, the titanium diffusion yields a lower increase of the refractive index, $\Delta n_e \sim 10^{-3}$ [7]. Nevertheless, LiNbO$_3$ itself possesses a quite high refractive index, typically ~2.2 [8], which means that in principle one could adhere much stronger field confinements in ridge waveguide geometries, by employ the high index step at the air-crystal interface.

25

The main problem to be faced to fabricate ridge waveguides, come first from the low etching rate of $LiNbO_3$ and secondly from the difficulty to find suitable masks with high enough selectivity to allow a deep etching . The solution I explored in my work consists in creating first a uniform proton exchange layer on the top of the substrate, so to weaken the crystal structure at the surface and enhance the etching rates. This allowed me to subsequently optimize the (reactive ion) etching of the substrate and achieve ridges with depths of several hundred of nanometers by simply employing a standard patterned photo-resist as etching mask. The PE top-layer not only allowed me to significantly enhance the etching rates of $LiNbO_3$ in the non-masked region, but also to automatically achieve the desired light confinement in the vertical direction in order to obtain a ridge waveguide.

The flowchart shown in Fig.4.1, summaries the various steps of the fabrication process which I developed in this thesis. They are discussed in more details in the following paragraphs.

LiNbO$_3$ wafer

Dicing and Cleaning

Proton exchange

photolithography

Reactive ion etching

Polishing
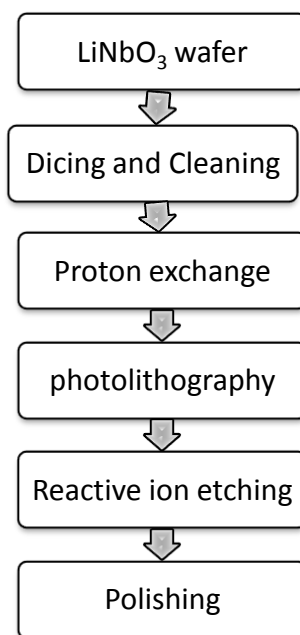
Fig.4.1 Waveguides microfabrication steps

The fabrication process, depicted in Fig. 4.2, starts by dicing the $LiNbO_3$ wafers into smaller samples, and then, after cleaning steps, I fabricated the uniform layers of proton exchange on the top and bottom sides of the samples. I then coated the PELN

26

samples with a uniform photoresist layer that I then patterned using photolithography techniques in the nanofabrication clean room. I subsequently transferred the photoresist pattern into the PELN substrates to the waveguides by means of reactive ion etching. With higher (~μm) ridges in LiNbO$_3$, one could achieve an index increase as high as $\Delta n = n_{LiNbO3} - n_{Air} \sim 1.2$ in the lateral (y) dimension, see Fig.4.2(c). If additionally proton-exchange is used a refractive index step is also introduced in the vertical direction (z). High-confinement of optical field can be then obtained over 2D cross section (y-z) as shown in Fig.4.2(c).

At the end of the fabrication, I removed the photoresist mask and the edges of the samples were polished in order to be able to couple light into the ridges and characterize the guiding properties.
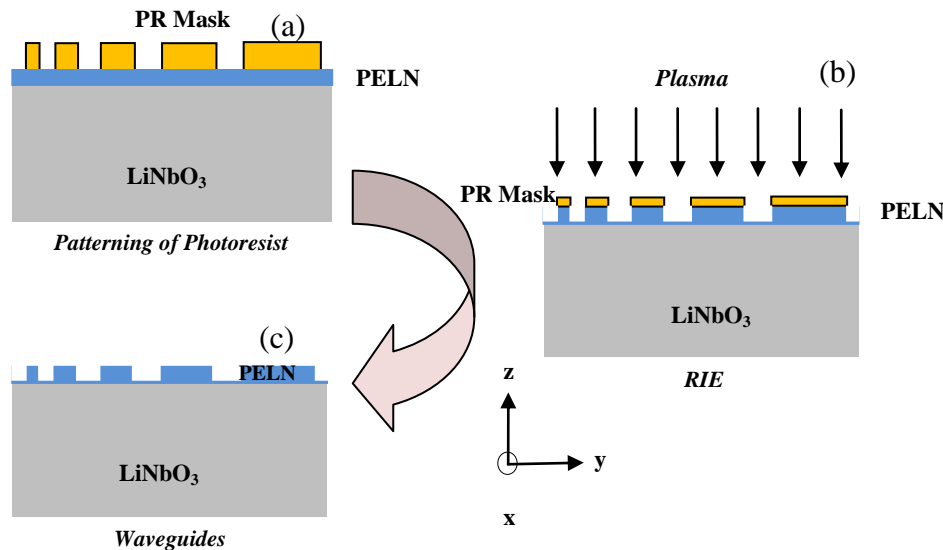
Fig.4.2 Sample before (upper) and after (right) the etching process and after removing the photoresist mask (lower).

4.3 Preparations of samples

The starting materials were produced from commercial providers, in the form of wafers of undoped and MgO-doped LiNbO$_3$ with diameter 3 inches and thickness of 500μm. A programmable dicing machine was used to cut the wafer. The size of the

27

samples was chosen to be 16mm × 11mm as shown in Fig.4.3. The ridges pattern data will be structured a long x-axis as propagation axis.
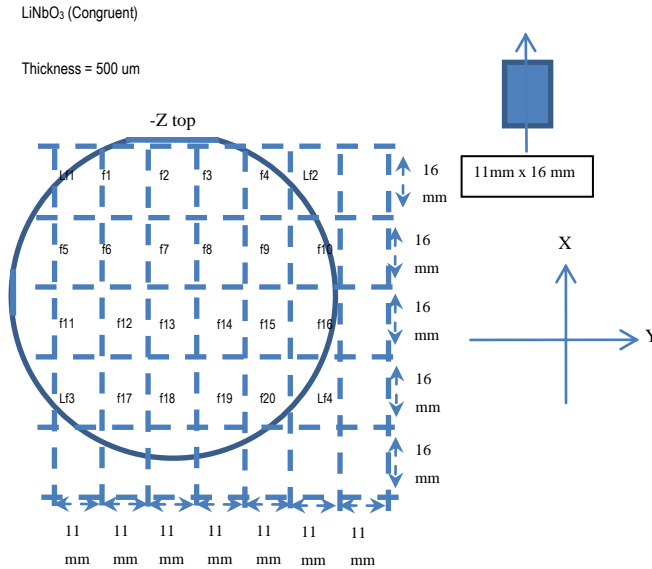
Fig.4.3 LiNbO$_3$ wafer dicing cut.

4.4 **Proton exchange (PE)**

The proton exchange is one of the techniques has been used for to make optical waveguides in lithium niobate [5]. It is a fast, simple and attractive to fabricate waveguides because of its relatively low temperature requirement to fabricate waveguides, Jackel was the first to report on it in 1982 [5]. The proton exchange increases the extraordinary refractive index by about $\Delta n_e = 0.12$[5][9], while it decreases the ordinary refractive index by a bout $\Delta n_0 = -0.04$ [5]. This anisotropic index change allows to guide the transverse electric (TE) mode in x and y-cut substrates and the transverse magnetic (TM) mode in z-cut substrates.

The proton exchange process refers to the ion exchange occurring at the surface of the wafer when exposed a heated acid bath. Many acids can be used as the proton source. Benzoic acid is most commercial acid that being used for PE, where the lithium ions at the crystal surface are replaced with the hydrogen ions coming from the acid bath to form a film of H$_x$Li$_{1-x}$ NbO$_3$. While the exact mechanism of is quite complex but in

28

principle it could be described through chemical reaction, when the Benzoic acid used as the proton source one could write the reaction as:

$$LiNbO_3 + C_6H_5COOH \leftrightarrow Li_{1-x}H_xNbO_3 + (C_6H_5COOLi)_x \qquad 4.1$$

The acidity of the bath determines whether complete or partial exchange has taken place, for the optical waveguides fabrication only partial exchange is necessary, by using undiluted Benzoic acid, which is relatively weak acid.

$Li_{1-x}H_xNbO_3$ system exhibits a complex chemistry structures, a number of phases have been identify, the phase transition can be characterized by a discontinuity of the index (Δn_e) and / or of the deformation a long axis perpendicular to the surface plane, they are indicated with α, κ_1, κ_2, β_1, β_2, β_3, β_4 [10]. I used beta phase, which exhibit the graded refractive index profile ~0.12, these phases can be plotting taking the stress tensor of the crystal ε_{33} as a function of step index Δn_e see Fig.4.4 below.
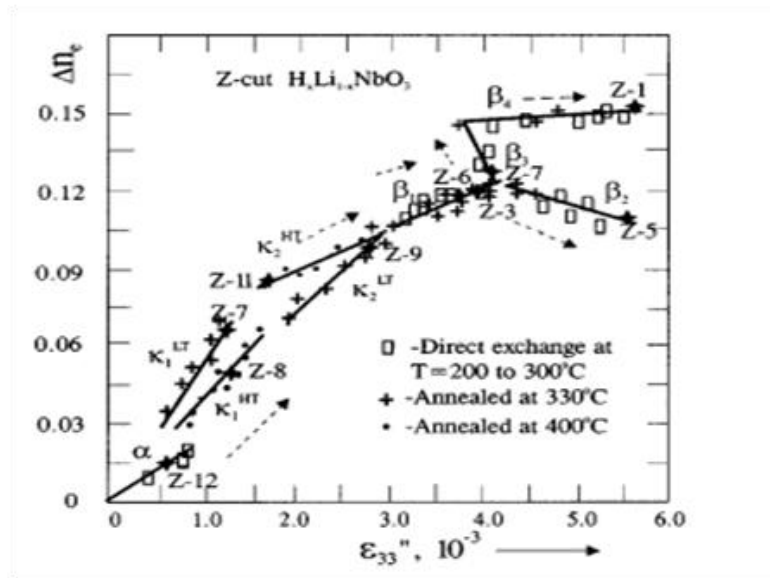
Fig.4.4 Deformation along crystal as a function of refractive step index in Z cut substrate [10].

The thickness of the PE film d_{PE}, is controllable by the process temperature and process duration. The diffusion of the proton in the substrate that forming the depth of the PE film layer can be described by the equation 4.2 as:

$$d_{PE} = \sqrt{4D_{PE}\, t_{PE}} \qquad\qquad 4.2$$

Where t_{PE} is duration of the process and D_{PE} is the constant of diffusion of the hydrogen in $LiNbO_3$ substrate surface, which is temperature-dependent. D_{PE} is displays exponential energy activation function dependence, and can be written as:

$$D_{PE} = D_0 \exp\left[-\frac{E_a}{kT_{PE}}\right] \qquad\qquad 4.3$$

where k is Boltzmann constant (k = 8.617343 $\times 10^{-5}$ eV K^{-1}), T_{PE} is the temperature of the process. D_o and E_a depend on the crystal orientation [5] [11].

Fig.4.4 below shows the thicknesses of PELN layer for different temperature values as a function of the process duration time.
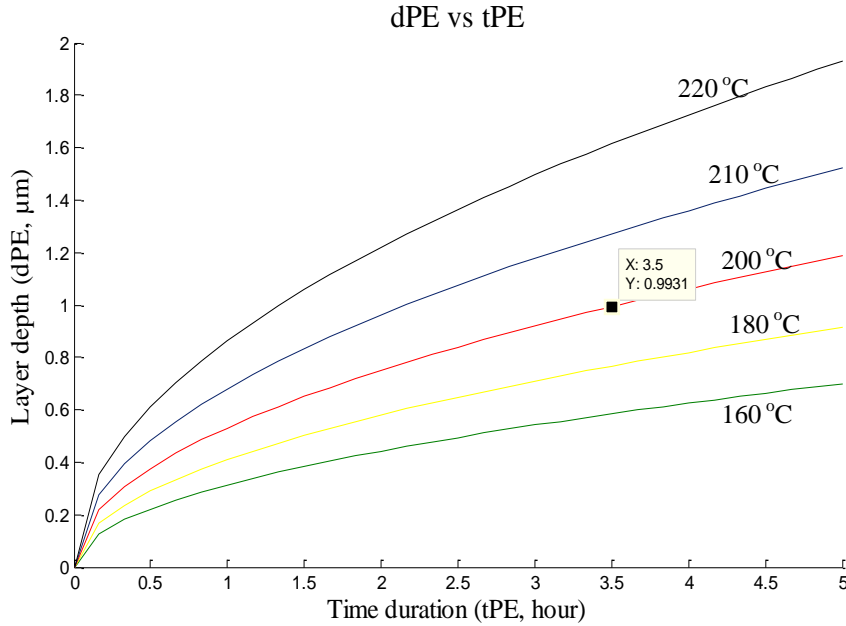
Fig.4.5 PELN film thickness as function of temperature and process duration time.

By using equation 4.2 and Fig.4.5 above, PE process conditions were: T_{PE} = 200, t_{PE}=3.5 h for the temperature and duration process time respectively, it were used to have a depth of PE layer ~ 1 µm, by taking the value of the diffusion coefficient as Do = 1.8$\times 10^9$ µm^2/h and energy activation function E_a = 0.987 eV, from Bortz [12].

Fig.4.6 shows schematic for the setup that was used for the Proton exchange process. The $LiNbO_3$ samples were put in the acid heat bath, fixed to the upper side of

30

the setup box, while the lower one contains the benzoic acid, which was heated with slowly gradient until 200°C. After the acid was melted the box was turned upside down and the reaction took placed for 3.5 hours, according to the equation (4.1), to reach the desired depth, then the process was stopped by turned it to the original side position, and cooled slowly till reach back the room temperature. The depth that was achieved from the process was measured using Metricon. See the fabrication results in 4.6.8 .

To remove the organic and inorganic contamination on the samples, that can attached to the surface from PE process, handling, or surrounding environment, by doing a normal cleaning process in an ultrasonic bath.
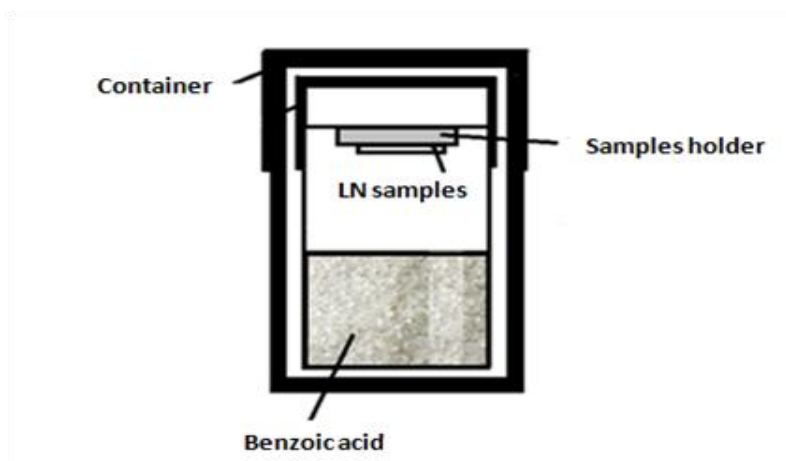
Fig.4.6 Proton exchange setup.

One way to determine the PE layer depth that achieved is to use the prism coupler methods that describe in chapter 2. A Metricon, that use the same technique, was used to measure the PELN layers depths.

References samples that have same PE condition process with other fabricated sampled were used to measure the PE layer, C-LiNbO$_3$ and MgO-LiNbO$_3$.

The PE:LN layers depth were measured for both Z faces of the sample with the Metricon and it was found to be about 1.4969 µm for C-LiNbO$_3$, while it is 1.0721 µm of MgO-LiNbO$_3$ samples.

Based on the experimental results, for the different depth I calculated the experimental the diffusion coefficients for both undoped and MgO doped liNbO$_3$ samples, using equation 4.1. This yielded that the diffusion coefficient for the proton

exchange process at 200 ^{o}C is $D_{PE} = 0.16$ μm^2/h and $D_{PE} = 0.071$ μm^2/h for C-LiNbO$_3$ and MgO-LiNbO$_3$ respectively.

4.5 Photolithography

Photolithography is one of the fundamental methods to fabricate microstructured devices. It is a way of patterning in where the substrate surface, first coated with photresist (PR) film and then exposed through a mask containing designed pattern using UV light. Fig.4.7 shows schematic typically photolithographic setup.
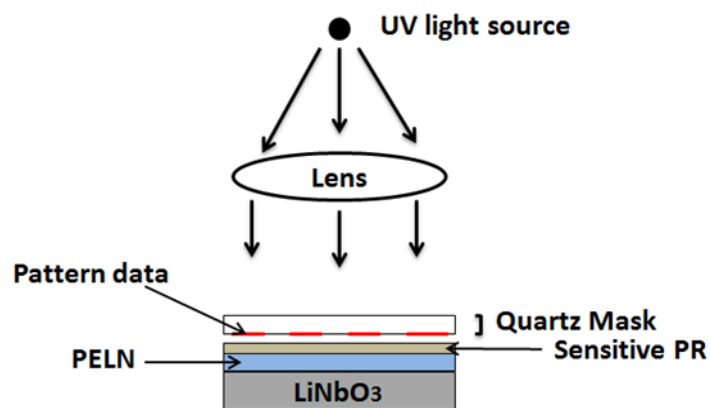
Fig.4.7 Photolithography setup.

The photolithographic process can be divided into three steps: the coating with PR, the UV exposure process and the development of the UV pattern in the resist. In the process, first a thin photoresist about 1.5 μm is uniformly spin on the substrate and then the PR pattern data transferred to the coated layer.

There are two types of photoresist, the positive when the exposed areas are removed, and the negative one when the exposed areas are remain after the development while the rest is removed as shown in Fig.4.8. Generally, the thickness of the photoresist spin layers depends on the viscosity of the resist and rotation speed of the spinner. Fig.4.9.(a) shows the curves from the data sheet of the resist S1818 that I used to measure the photoresist thickness. After spinning to vaporize the solvent resist film for better adhesion to the substrate, the photoresist was prebaked in an oven at 100℃ for 1 hour with slow heating and cooling cycle to avoid not reversed the substrate polarization.
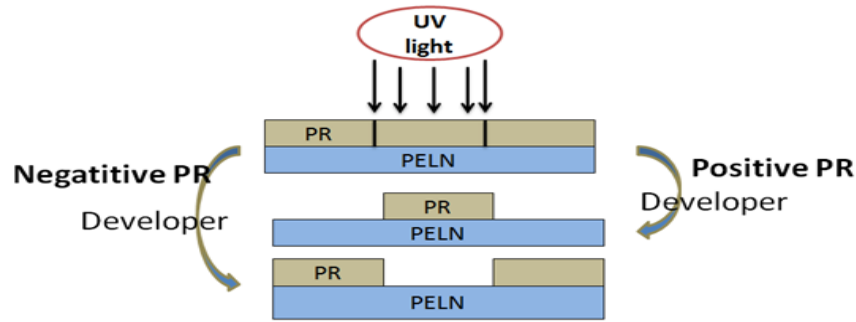
Fig.4.8 The negative and positive types of photoresist.

The mask that I used for the resist exposure was made by chrome on quartz. A Karl Suss MA4 mask aligner with a highly pressurized mercury lamp and a peak spectrum at a wavelength of 365 nm was used ultraviolet (UV) exposure. The ridge design pattern of the mask used for the exposure had 12 set of ridges bands 10 mm long with varying width from 1:1:12μm separated by 40 μm as shown in Fig.4.9 (b).

(a)   (b)
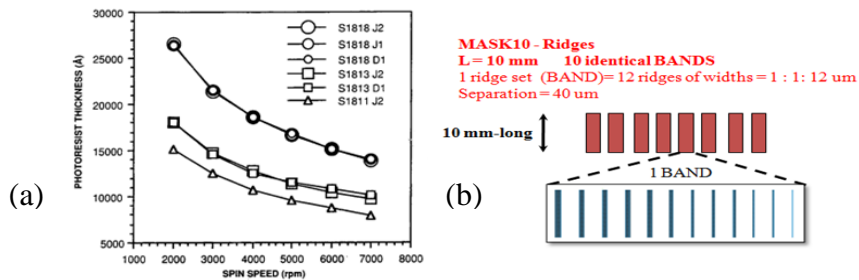
Fig.4.9 The thickness of the photoresist as a function of spin speed for Micropost S1800 series [13] (a). The Mask used to write the lithography ridges pattern (b).

After exposure, the samples was dipped in the developer solution to remove the exposed areas, the exposure and dipping times were determined by eye estimation to have a good pattern, Fig 2.10 shows the resist pattern after the development process, and Table 4.1 gives typically values and conditions used in the process.

Fig.4.10 The photoresist pattern after the development.

Table 4.1 the values that used to pattern the PR data

Photoresist type	Positive type (S1818)
Spinning time	6000 r/min
Baking duration	1 hour (slowly gradient heating in oven)
Exposure time	3.5 s
Developer time	80 s
Post-baking duration	1 hour

After the process, the samples were rinsed in DI water, dried with compressed air, and post baked to further increase the resistance against etching. Fig.4.11 shows the widths parameters that were measured and Table 4.2 presents the results for the pattern structures values that were obtained.
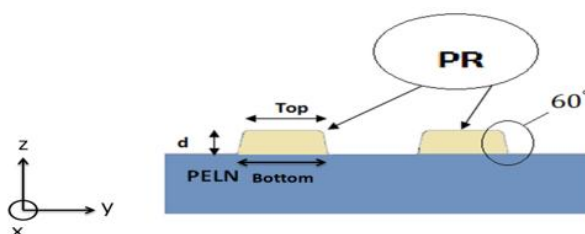
Fig.4.11 The photoresist pattern

Table 4.2 PR pattern structure before the etching process in μm

Sample		1	2	3	4	5	6	7	8	9	10	11	12
C:LN	top	--	1.2	1.4	2.4	3.1	4.3	5.2	6.2	6.8	7.8	8.6	9.7
(-Z)	bottom	--	2.1	3.1	3.9	4.9	5.9	6.9	7.7	8.7	9.5	10.6	11.4
C:LN	top	--	1.1	1.7	2.4	3.2	4.2	5.1	6.0	6.7	7.9	8.7	9.6
(-Z)	bottom	--	1.7	2.9	3.7	4.7	5.8	6.9	7.6	8.4	9.5	10.4	11.4
MgO:LN	top	--	1.3	1.6	2.1	3.3	4.2	5.1	6.1	7.0	7.6	8.6	9.9
(+Z)	bottom	--	1.9	3.1	3.9	4.8	5.8	6.9	7.8	8.8	9.5	10.7	11.8
MgO:LN	top	--	1.6	1.7	2.3	3.2	4.3	5.0	6.0	7.0	7.7	8.9	10.0
(+Z)	bottom	--	2.1	2.8	4.0	5.0	5.9	6.6	8.0	8.7	9.5	10.6	11.4

4.6 **The reactive ion etching**

Many dry etching techniques are available which they use gaseous etchants, such as Magnetically enhanced reactive etching (MERIE) [14] and Electron cyclotron resonance (ECR) etching [15].

The reactive ion etching (RIE) is a simple easy controllable way to achieve a good etching rate and to avoid isotropic processes in chemical wet etching. Good results are expected by using the RIE and relatively large selectivity to enhance high structure depth ridges and enhance anisotropy for vertical etching.
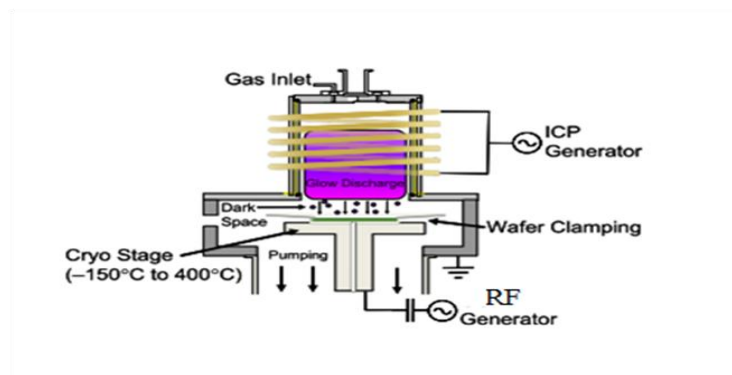
Fig.4.12 Schematic RIE system.

A schematic RIE chamber in the Fig.4.12 above is consist of a Vacuum chamber, RF power as lower electrode plate (cathode) in same time it is work as sample holder, an upper electrode (the grounded chamber) and the ICP generator.

The plasma system generates electron, ions, and free radicals (ions, atoms, molecules with unpaired electron, which may can have positive, negative or zero charge) such as fluorine the one I used to attack the surface chemically. The Plasma is generated by applied a strong Radio frequency, typically 13.56 MHz, the RF power supply is attached to the electrode for to control the ion bombardment energy independently.

In appearance of low-pressure condition, and exist of fluorine (CHF_3) and inert (Ar) gas. The oscillating electric field ionized the gases molecules due to collisions between the accelerated electrons and the etchants gases. During the process, any electrons hit the chamber wall grounded, however the others stripped from the electrode plate (wafer table) give a large positive charge about few hundred Volts, near the surface region, this region called sheath reign or dark space. Then the relatively large voltage

difference between the plasma and the RF electrode is tend to drift the negative ions toward the wafer plate which cause the etching when reach the substrate surface.

The ions in the plasma can be accelerated by sheath field to high energies while flowing to the substrate lead to energetic ion enhanced processes.

The ICP system is more effective at ions generation and a useful to have control to the ion density, for the little loss ions in the chamber wall, and it is possibility to operate at low pressure which make the mean free bath of ions rather long.

4.6.1   The etching mechanisms

The Plasma etching mechanisms can be divided into four classes depending on the type of interactions introduced:

1. The mechanical etching, which is due to ions bombardment.
2.   The chemical etching, which occurs due to neutrals (atoms/molecules with no charge) causing surface reactions.
3. The ion enhanced energetic etching.
4. The ion enhanced inhibitor etching.

Fig.4.10 and Fig.4.11 below show the main basic etching mechanisms adapted from [16]
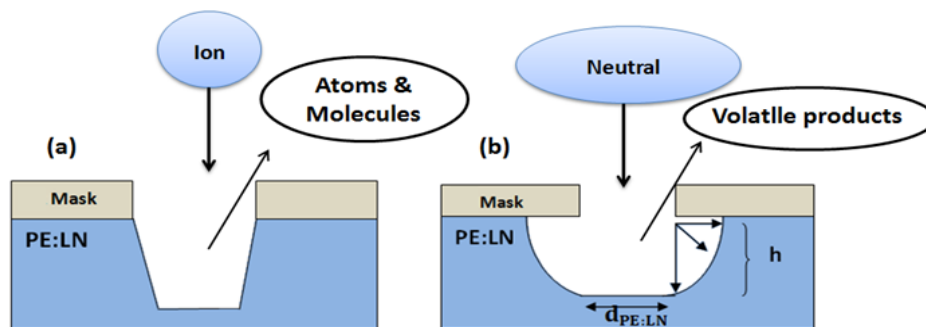
Fig.4.13 The etching basic mechanisms, mechanical (a), Chemical (b) adapted from [16].

In the first type see Fig.4.13 (a) above, the momentum transfer from accelerated ions in the plasma removing material from the surface of the substrate and throws it across the reactor chamber. This mechanism is called sputtering. The positive ions such as (Ar^+) ions are propelled into the surfaces by the negative going potentials at the edge of the plasma. This mechanism requires low pressure and long free mean path, to let the

36

materials to leave the vicinity of the surface without being backscattered and re-deposited. Sputtering is anisotropic process but has low selectivity.

In the second type of the mechanisms, the chemical one, see Fig.4.13 (b), the active gas phase species, which usually are free radicals, and led to high chemical reactions, e.g. fluorine atoms, in the plasma are, encounter the substrate surface, forming volatile products. It effect is to etch and remove the surface substrate material in the same way as the common chemical reactions occurring during wet etching, and usually the process is therefore attack non-directional since the ion bombardment plays no role, this produces isotropic circular etch profiles and etching undercut areas, except for some preferential etch direction crystal. Its chemical reaction and the etches could guarantee extremely high selectivity.
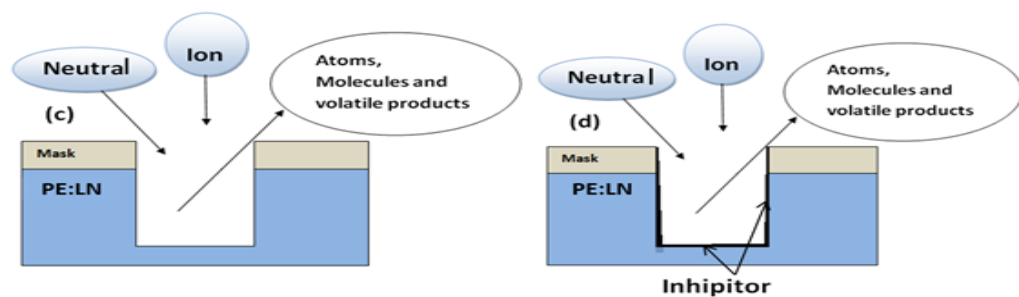
Fig.4.14 Energy assisted plasma (c) and ion inhibitor driven assisted mechanism (d) adapted from [16].

In the third type of etching, the ion enhanced energetic etching see Fig.4.14 (c) above, the energy ions, which act mechanically, are work to assist the plasma chemical etching. The ions job is to damage the substrate surface and make it reactive and ready for incident naturals.

The fourth mechanism that use on etching is the ion enhanced inhibitor etching see the previous Fig.4.14 (d). In this mechanism, ions are interacting with the second ingredient films that may coat the substrate surface and its vertical sidewalls. These films can come from other processes, e.g. inhibitor species from plasma or the non-

volatile process. The mechanism is work to solve the stop of the interaction with the plasma and the substrate surface let to continuing the etching process.

4.6.2   Anisotropic plasma etching

Neutrals and the ions can work together in synergy to achieve high material removal rates, exceeding the sum of the separate Sputtering and the chemical interaction attacks. The neutrals directed and assisted by the ions bombardments, to cause the anisotropic plasma etching.
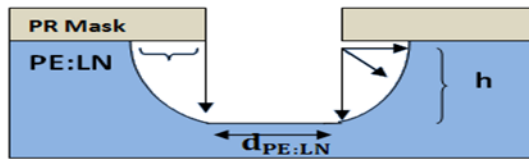
Fig.4.15 The etching degree of anisotropic.

In the etch profile shown in Fig.4.15 above. The anisotropic etch degree is generally can be defined according to the relation:

$$D_A = 1 - \frac{|B|}{2h},$$

Where d_{PR} is the opening of the PR mask, d_{PELN} is etching layer process window and h is the depth of etched layer. The anisotropic etch degree varies between zero and one:

$0 \ (\equiv \text{Isotropic}) \leq D_A \leq (\equiv \text{anisotropic})$, thus $B = d_{PELN} - d_{PR}$, equals to 2h, for an isotropic etching and zero for a highly anisotropic one (vertical walls).

To have anisotropic etching, the plasma supplies both reactive etchants and the energetic ions, the ions bombardment weaken the surface, helping the plasma chemical reaction, these plasma chemical reactions can be described through in the few steps shown in Fig4.16. The reactive species and free radicals generated in the plasma reach the surface. (1). Then ions and the neutral species are driven by the diffusion (2) and are absorbed at the substrate surface (3). After that in step (4), the reaction at the surface takes place. The neutral species react with the material forming volatile products (Li+ 4F→LiF$_4$), LiF$_{4(ads)}$, then desorption from the substrate surface (5) and diffuse in gaseous forming LiF$_{4(gas)}$ [6].
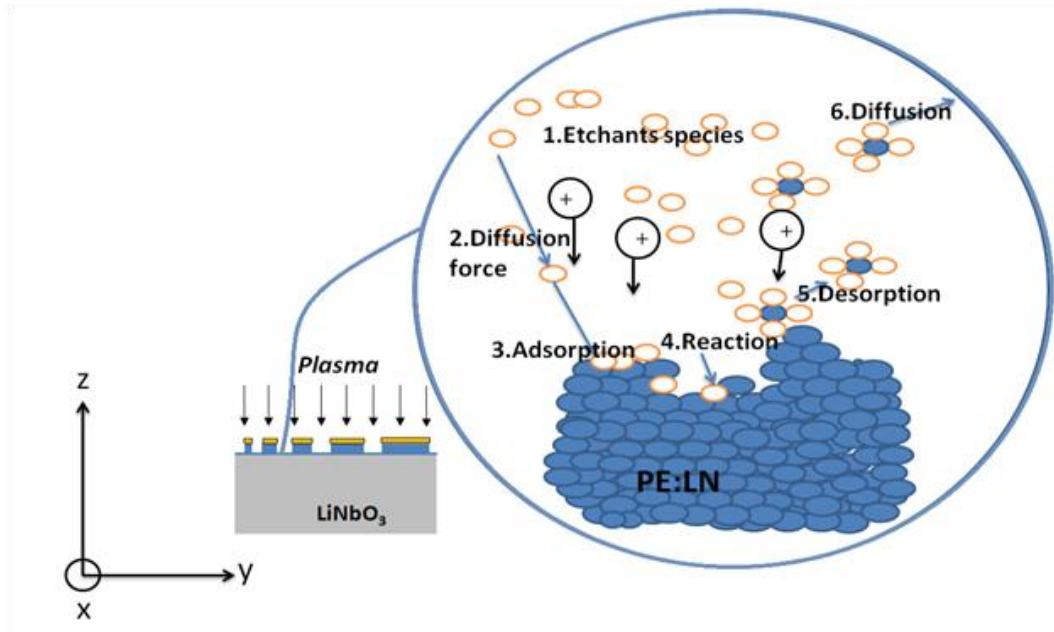
Fig.4.16 Surface chemistry dry reaction etching steps.

4.6.3   The etching process in LiNbO₃:

Plasma etching process is characterized by its selectivity, etch rate, uniformity, and final surface quality. In my work, I explored the effect of several central parameters to optimize the etching process, namely the reactor chamber pressure, radio frequency RF input power, inductive coupled plasma (ICP) energy, gases flow rate and process temperature.

Many recipes were studied, while working to enhance the etching rate. The above parameters influence diametrical changes in the process results. See Table 4.3 it shows some recipes I used looking for high selectivity working recipe with easy to remove the photoresist after the etching, it shows the parameters affect, there are many recipe with successfully easy to remove the PR. later in this chapter, I reported my work around the final recipe that have peak in the selectivity, this study beside to investigate the final recipe, also describes the influence with the parameters, the RIE process, it shows how perfect same results, with same recipe using plasma etching can obtain.

Table 4.3 Some selected recipes shows the parameters influences and their out come

Pressure (mtorr)	CHF$_3$ (sccm)	Ar (sccm)	ICP (W)	RF (W)	Time duration (min)	Etching rate (nm/min)		comments
						LN	PELN	
20	20	2.5	200	50	10	2.39	12.80	Hard PR
20	30	2.5	200	50	10	----	5.24	Hard PR
10	20	2.5	200	60	10	6.29	32.59	Hard PR
10	70	2.5	200	100	10	5.06	39.26	Hard PR
20	90	2.5	200	100	10	----	20.70	Hard PR
40	70	2.5	200	100	10	----	-----	Baked PR
20	90	2.5	300	100	10	----	46.00	Hard PR

4.6.4 The etch selectivity

The selectivity is the ratio between the etching rate of the layer to be processed and the etching rate of the mask. A good selectivity ensures that the mask will not remove during the process, which is important to achieve the required depth. In our case, the process layer is PELN part and the mask is our photoresist part. Thus, the selectivity is defined by the equation below

$$\text{Selectivity} = \frac{\text{Etching rate of PELN layer}}{\text{Etching rate of PR}}$$

To maximize the selectivity the reactive species need to have the following properties:

1. Low etch-rate of the mask material over the layer being etched.
2. Low etch-rate of the materials under the layer being etched (etch stop layer).
3. High etch rate for the material being removed.
4. Excellent etching uniformity.

To calculate the selectivity we defined the etching rate as a measure of how fast the material is removed in the etch process. This can be given by the equation below

$$\text{etching rate} = \frac{\text{the thickness before etch} - \text{the thickness after etch}}{\text{Etching time}}$$

40

4.6.5 Pressure effect

The pressure influences the major phenomena that control the plasma etching. When the pressure is low inside the etch chamber, there will be less reactants and a long free path distance for the ions to move. Then by increase the potentials across the sheath this can make the ions carry a higher energy momentum. These causes mainly sputter etching. By increasing the pressure, one can on the other hand reduce the mean free paths of the ions. The more frequent collisions between gaseous species lead to more free radicals, thus at relatively high pressures the etch process will be mostly chemical.

However, the high ions energy is undesirable because of the decrease in selectivity associated to the increase in the ions energy.

First I explored the pressure value on etching the $LiNbO_3$ samples, many values were tested, i.e. 10, 20 and 30 mtorr, while keep the other rest parameters fixed, as 70 sccm for CHF_3, 2.5 sccm for Ar, 200W ICP and 200 ^{o}C for the chamber temperature, for period of time 20 min each recipe. The recipe with the less pressure value gave a profile depth 120 nm while the rest gave very low depth and unclear profile. Thus, I sat my chamber to have low-pressure values, which agree with literature [16], and I used 10 mtorr for the final etching recipes, to have longest free path length for etchant species. Moreover, I faced difficulties to ignite the plasma with pressure value low than selected one.

4.6.6 Effect of Radio frequency and ICP powers

The Radio frequency RF power is applied to the cathode plate (the lower electrode) to generate the plasma, and to influence the mechanical etching. An increase in the RF power mainly cases increase on the energy of the bombardment ion.

I investigated many values for the RF power, with different etching recipes parameters with RF power values, e.g. 50W and 70W; I found etching rate was 5nm/min and 20nm/min respectively.

A jump on the etching rate up to 30nm/min was achieved by increase the RF value. The highest etching rate achieved at 100W, and when I increased the RF power above 100W, e.g. 130W and 150W while the other parameters remain fixed, I observed no significant etching rate, but instead the ion bombardment high energy heated the

sample surface and baked the photoresist mask, making it hard to remove it. I used 100 W for the RF power value in my start point with 10 mtorr pressure, to optimize my etching rate with ICP power and gaseous etchant parameters.

The Inductive Coupled Plasma ICP power increases the vertical magnetic field through the plasma, which increases the number of electron-gas collisions number, and therefore creates more ions. As a result, the ion density increased and more species that are reactive will be sent to the substrate, which increases the chemical component of etching. The advantage of using ICP RIE is that one could increase the ion density numbers without increasing the energy. This is useful to avoid photresist baking, and make it easy to remove.

As it shown in Fig.4.17, to investigate the peak using my ICP parameter, I performed serial paths for the impact of ICP power and the etch rate of mask (red points) and substrate (blue points).
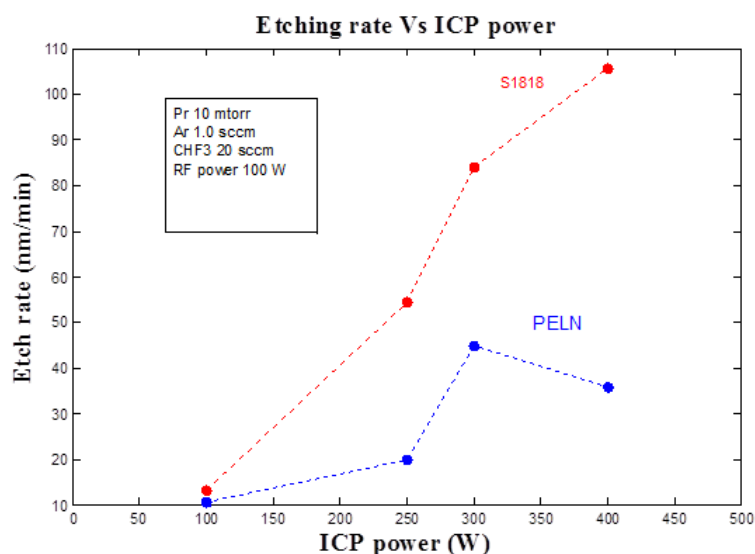
Fig.4.17 Etching rate as a function of ICP power.

By increasing, the ICP power starting from 100 W an increase in the etching rate was registered, in both PELN layer and the Photoresist registered. This is while the other recipe parameters are fixed specifically the pressure was 10 mtorr, the Ar gas flow was 1.0 sccm, the CHF$_3$ gas flow 20sccm and the RF power 100W. At a value of 300W, I observed the highest etching rate, for the PELN layer. By increasing the ICP power further, a decrease on the etching rate was registered for PELN layer, while the mask

42

etching rate increases, which means that above 300W the selectivity will decrease (photoresist mask will be removed faster).

4.6.7   Etching rate and the etchants gases

One of the limits in the etching of $LiNbO_3$ with Fluorine gases is due to the redeposition of LiF, practically on the surface and sidewalls of the etch trenches see Fig.4.14(d), which reduce etching rates and causes non-vertical etched walls [17]. A solution to enhance the etching rate is to reduce the lithium concentration in the material. Using the PELN process, as I discussed before in chapter 2 weaken the substrate surface by exchange process reaction that I will describe it later here in this chapter, and therefore it likely also help to reduce the impact of LiF redeposition.

The fluorinate gas I used for my experiments was CHF_3, and as I discussed before, in order to achieve synergistic action (to get anisotropic deep etching) of the mechanical and chemical I used a mixture of CHF_3 and Ar gases.

For the chosen operating pressure 10 mtorr and RF power 100W, I studied the effect of the CHF_3 concentration of the etch rates of PELN and Photresist mask S1818.

Fig.4.18 shows the results obtained for a fixed Ar gas flow at fixed value 1.0 sccm at ICP 300W, RF 100W and pressure 10 mtorr, with different CHF_3 concentration.
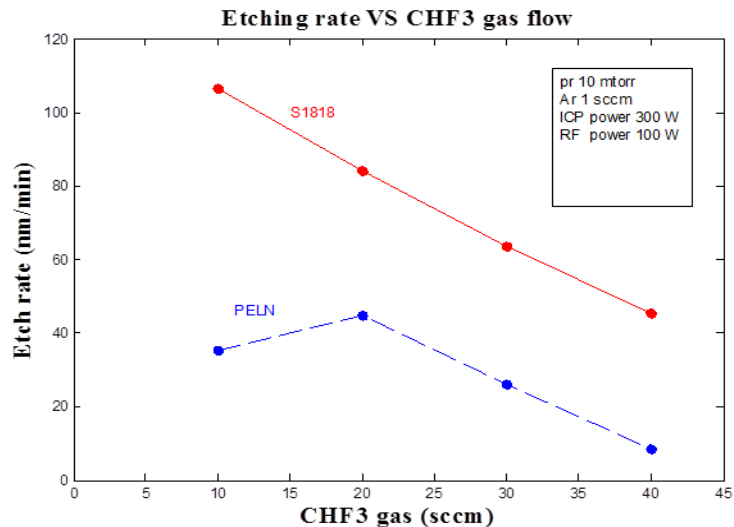
Fig.4.18 Etching rate as a function of CHF_3 gas flow.

CHF$_3$ is used to produce in the plasma the chemically reactive species, which is fluorine to etch and remove the target material PELN. By increasing the CHF$_3$ gas flow rate, a increasing on the PELN layer, see the blue dashes line, likely the photoresist mask decreasing was registered. At a value of 20 sccm, I observed the highest etching rate, for the PELN layer, this means the amount of the chemical reactive species work effectively. By increasing the gas flow rate further, a decrease on the etching rate is registered for PELN layer, while the mask etching rate keep decreasing, that because adding more species decrease the mean free paths inside the reactor chamber, which lead to less energy species react substrate surface.
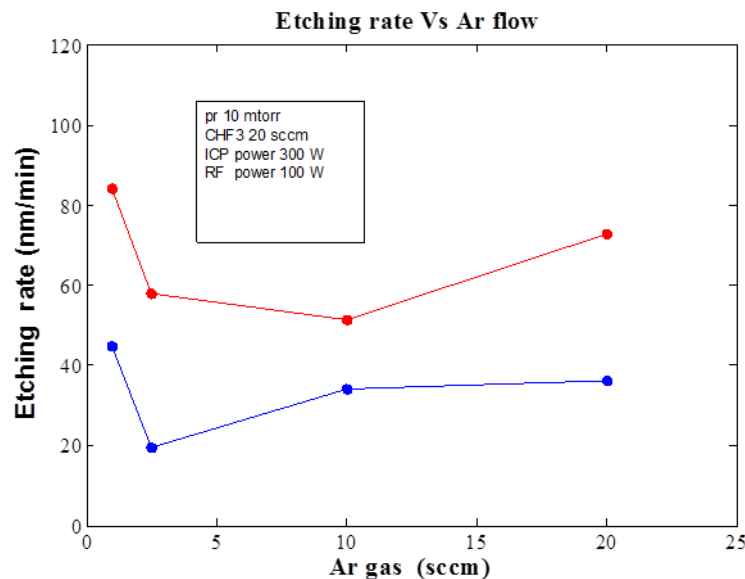
Fig.4.19 Ar gas affects on PELN and mask photo-resist.

For the chosen operating pressure 10 mtorr and RF power 100W, ICP power 300W, and CHF$_3$ 20 sccm, I studied the effect of the Ar concentration of the etch rates of PELN (blue line) and Photresist mask S1818(red line).

Fig.4.19 shows the results obtained with different Ar gas concentration. The highest etching rate registered for both the PELN layer and the photoresist mask at the Ar gas flow rate 1 sccm, and by increasing the gas flow rate lead to the increase reactive species inside the chamber which give a reduce to mean free paths for the etchants. Therefore, a decrease on etching rate was observed. Uses of the 1 sccm as working point

44

help to avoid the increases of the substrate thermal temperature, which cases baking of the photoresist and make it hard to remove.

4.6.8 Temperature effect

The RIE process in generally lead to heating of the samples, because the accelerated ions bombardment hit the surface with high energy and due to the chemical reaction between the reactive species and the substrate surface. During my studies, I discovered that the temperature of the sample during the RIE has a profound influence on etching. It is important in the process to distinguish between the gas temperature, which is a complex function of local power input such as heat transfer and transport phenomena, and the substrate surface temperatures. The surface temperature is play role on the substrate etching, heating it lead to a baking layer surface, that may cause a decrease on etching rate same as accurse hard photresist that difficult to remove with normal cleaning solvent and process, e.g. acetone, removers, and plasma O_2 cleaning.

I manage to enhance the etching rate and remove the hard photoresist see Fig.4.20, using the acetone when cooling the substrate by controlling the backside of the sample being etched. I used a tiny liquid layer on back of the substrate and simply fixed it to the holder (quartz plate).

I studied many different temperatures values as working process temperature (47^oC, 37^oC, 29^oC, and 20^oC) the best working degree temperature for my recipe to etch the PELN layer using a photoresist mask S1818 is 20^oC.

Fig.4.20 Hard Photoresist.

4.6.9 Final recipe

By study the recipes results using the above parameters, and by investigate the selected recipe, I used it and then report my study results as you will see later.

Table.4.4 below shows the parameters values of the recipe that used for etching lithium niobate samples. Both undoped and MgO doped samples, $+Z$ and $-Z$ faces were etched together, after an O_2 Plasma ashing applied to clean the RIE chamber for to clean the chamber from any other gases may remain form any previous process, because existence of any other etchant gases species will change the chamber conditions and so changing my recipe and etching process.

Table.4.4 The selected recipe values used on etching

Pressure (mtorr)	RF (W)	ICP (W)	CHF$_3$ (sccm)	Ar (sccm)	Temperature In Celsius	Time (min)
10	100	300	20	1	20	16

4.6.10 Waveguides Fabrication

In this section, the results on the fabrication of the waveguides PELN are reported. These results are concern both undoped and MgO doped Lithium niobate samples for both +Z and –Z faces. To which I applied same processing conditions described in the previous paragraphs (with RIE recipe of 10 mtorr as chamber pressure, 100W for RF power, 300W for ICP power, 20 sccm as CHF$_3$ gas flow rate, and 1 sccm as Ar gas flow rate in affixed chamber temperature 20°C).

Standard characterization of the fabricated waveguides; by optical microscope inspection and surface profilometer, then further complemented by prism-coupling and at AFM measurements, the former was used to precisely determined (in non destructive way) the depth of the PE layers, while the latter was used to investigate the uniformity and surface quality of the waveguides at nanometer scale. These characterizations are important for future optimization of the waveguides process, since they determine, e.g. the waveguides losses and confinement properties.

To determine the etching rate and to calculate the selectivity, first I measured the depths of the photoresist mask layers before the etch process, using the profilometer, and then I performed the RIE by using the select recipe. After the RIE, I measured the height of the features before removing the photoresist, and then after I removed the

photoresist mask I measured the depths of etched feature on the PELN. Table.4.5 shows the original thickness of the photoresist (deposited at a rotation speed of about 6000 rpm), the thickness of the photoresist remaining after etching process, and the heights of the ridges.

Table.4.5 Ridges measurements profiles

Sample		Process face	Thickness of PR befor RIE (nm)	Remain PR (nm)	PELN etching depth (nm)	Etching rate
PE	C:LN	−Z	1550	130	500	31 nm/min
		+Z	1485	210	480	30 nm/min
	MgO:LN	−Z	1570	310	305	19 nm/min
		+Z	1415	365	290	18 nm/min

I can notice that, in an agreement with expectations, the etch rates with fluorinated RIE are slightly larger on the −Z face, compared to +Z one, for both undoped and MgO doped LiNbO$_3$. The diference between the etching rates was 9nm/min, these different values according to the sample orientation and the positively charges electric field, which form a barrier against the etch process.

On the other hand, from the summarized data it is also apparent that the etching of MgO:LN is lower than that of the undoped material (by 30%).

Moreover, about 84 nm/min and 72 nm/min was the photoresist etching rate respectively. The above results give a selectivity of 0.36 and 0.25 for both undoped and MgO doped LiNbO$_3$ respectively.

The etched patterns had sidewalls angles of 60 degrees for both undoped and MgO doped proton exchange LiNbO$_3$ was regardless of the depths and widths of the etching, neither face ($\pm$ Z) nor the MgO doping. The average results for the sidewall angle measurements are summarized in Table.4.6 .

Table.4.6 Ridges sidewalls angles before the etching process.

	Sample	Process face	Sidewall angle (in degrees) before etching
PE	C:LN	−Z	61
		+Z	59
	MgO:LN	−Z	63
		+Z	60

The data above were obtained by measuring the top and the bottom of the feature widths along photoresist pattern with the profilometer and then calculating the slopes and at last taking the average value for each sample.

One way to investigate the surface roughness in nanoscale is to use an Atomic Force Microscope (AFM) setup, Fig.4.21 shows a schematic typically to that used, which the main part consist of sharp probe, laser diode, photo detector, and piezoelectric scanning system, and a computer.
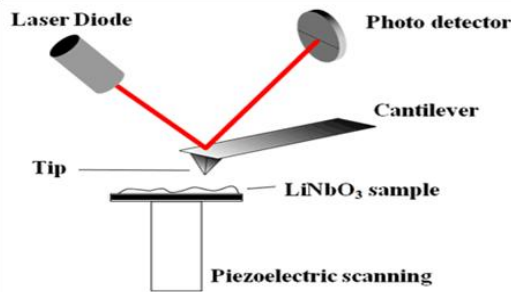
Fig.4.21 Schematic setup typically used at AFM technique.

AFM is a technique which can provides a three dimension profile of the surface on Nanometer scale, by measuring forces between a sharp probe (less than 10 nm), at very short surface distance (0.2−10 nm probe sample separation). The probe is support-ed on a flexible cantilever. Using tapping mode method, in which the probe "taps" on the surface during the scanning, and contacting the surface at the bottom with a constant oscillation amplitude swing, the tip gently touches the surface and records the small

force between the probe and the surface to images the substrate surface. Fig 4.22 showing 3 output images scanned by an AFM for C-LiNbO$_3$ –Z face.

Fig.4.22 AFM pictures of tapping mode scanning of C-LN waveguide (Height, amplitude and phase signal respectively).

This further investigation with AFM techniques, which is confirmed essentially the above measurement on the angles and additionally allowed me to evaluate the sidewalls roughness. The interplay of the high resolution in both lateral and orthogonal directions and the non-destructive approach will give both high fidelity scans of the surfaces and very accurate analyses of the roughness.

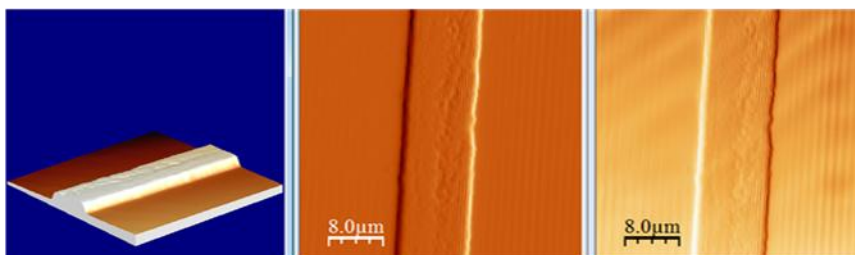First by calculating the feature of the non- processed samples, the proton exchange ones. The table below summaries the roughness results of these samples:

Table.4.7 Roughness values for the non-processed samples

Sample	+Z (nm)	–Z (nm)
LN	2.15	3.75
MgO:LN	3.91	2.15
PE:LN	2.35	3.63
PE MgO:LN	3.84	2.68

For the virgin congruent LiNbO$_3$ the roughness is very low (~few nm) and basically it is mainly due to topographic features of the final polishing of the wafers at the end of the industrial growth and wafer cut process. A slight difference depending on the polarization of the sample was measured, i.e. 1.5 nm deepest structures in the –Z face at undoped sample and 1.5 nm deepest structures at +Z face in MgO doped sample, but no appreciable variations due to PE were measured, i.e. for the undoped –Z face of 0.12 nm

49

and +Z face of 0.2 nm, while in MgO doped sample it was of 0.53 nm at –Z face and 0.07 in +Z one.

The other area that was scanned is the sidewalls area. This area is one of the highest interests in my work; as a matter of fact the roughness of the sidewalls is a key aspect for the optical properties of the waveguides in particular the guided mode losses.

The highest part of the ridges, i.e. the "Top" areas, which were protected by the photoresist during the etching process, should be preserving the original roughness of the PE samples. Also the reading with AFM registered for the areas between the ridges, i.e. the "Bottom" areas, which were etched during the process, gives an indicator of roughness damage produced by RIE on the substrate ($\Delta\delta_{PELN}$).

To analyse the roughness in the specific areas mentioned above, I used the RMS values. For the means I used additional none preceded ($\pm$Z) LN samples as reference for the roughness. By scanning and analyzing the features of the etched samples surfaces, and comparing them to the reference samples. Fig.4.23 is presented a 3D sketch of the waveguide in order to identify the areas of interest; these pictures were obtained by using the data we measured from the sample MgO- LiNbO$_3$.
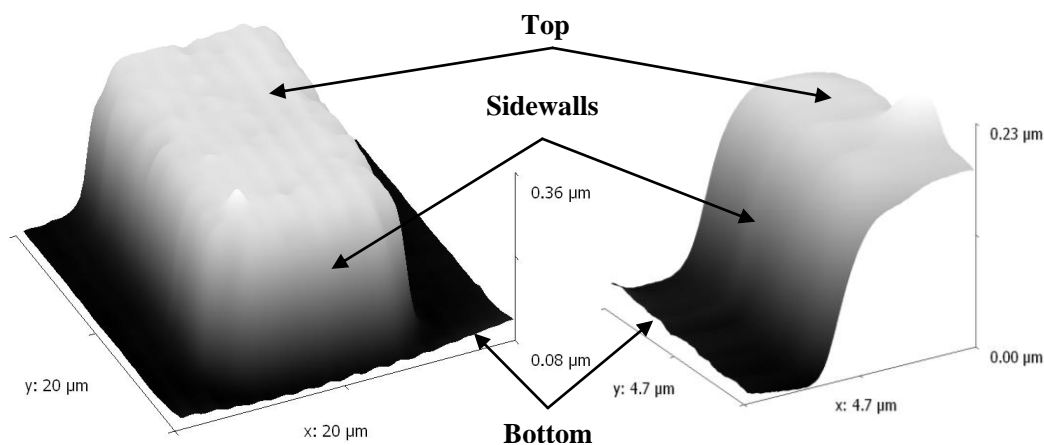

Fig.4.23 Top, bottom and Sidewalls MgO- LiNbO$_3$.

By scanning the top, bottom, and sidewalls for the proton exchange undoped and MgO doped samples for both ($\pm$Z) faces. A summarize to the results obtained will found in Table.4.8 .

Table.4.8 The roughness summaries results of the ridge samples.

Sample		Process face	Top	Bottom	Sidewalls
PE	C:LN	–Z face	3.71 nm	1.36 nm	4.03 nm
		+Z face	2.19 nm	1.57 nm	3.94 nm
	MgO:LN	–Z face	2.95 nm	1.81 nm	5.40 nm
		+Z face	3.57 nm	0.55 nm	4.73 nm

The roughness at the top of the ridges, Table.4.7 compares with the one of none processed samples showed in the Table.4.6. This makes sense, since the top side of the ridges were protected by the photoresist during the etching, there should not be any appreciable variation of the roughness in comparison with none processed samples. This also confirms the perfect removal of the photoresist mask with our standard (acetone) cleaning process after the RIE.

The ridges waveguides fabricated in this C-LiNbO$_3$ substrate samples are roughly having a lateral sidewalls slope of $\sim 60\,°$.

The bottom etched side also here is the smoothest one for both undoped and MgO doped samples. The reactive ion etching process seems to reduce the roughness by more than 40 % which is a positive outcome. The roughness of the sidewalls is higher than in all the other areas and it seems not to be dependent on the polarization of the substrates. In fact the sidewalls are the target of reactive species and chemical reactions such as redoposition of LiF.

4.7 Ridges waveguides

The fabrication technique that is report in this master thesis achieved a 3D configuration of ridges waveguides, the PELN layer was not completely etched, and still

there is a layer on top of the LiNbO$_3$ substrate. The ridges have sidewalls angles of about 60° this can be shown in schematic Fig.4.24 below.
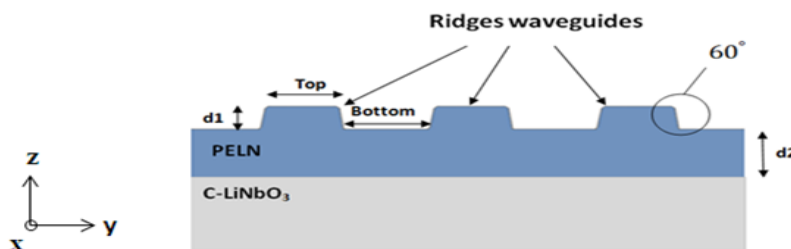

Fig.4.24 Schematic C- LiNbO$_3$ ridges waveguides.

For the undoped LiNbO$_3$ sample the PELN layer depth of about 1.5 μm, by the RIE technique a depth of about 500 nm and 480 nm for both –Z and +Z faces respectively, and sidewall angle ~60° and surface roughness about 3.71nm and 2.19 nm on the top (un etched areas), 1.36 nm and 1.57 nm at the bottom (the etched areas), and on the sidewall about 4.03nm and 3.94 nm for both –Z and +Z faces respectively.

While for the MgO doped LiNbO$_3$ sample the PELN layer depth of about 1.0 μm, by the RIE technique a depth of about 300nm of about 200nm less than the undoped one, and same sidewall angle ~60° and a surfaces roughness about 2.95nm and 3.57 nm on the top (un etched areas), 1.81nm and 0.55 nm at the bottom (the etched areas), and on the sidewall about 5.40nm and 4.73 nm for both –Z and +Z faces respectively.

4.8 **Summary of the fabrication**

Lithium Niobate is a hard and relatively inert material, hence it is quite difficult to etch. With the reactive ion etching (RIE) technique developed for this propose, I obtained 500−300 nm depths in LiNbO$_3$ substrates, with a simple photoresist mask by using high-density plasma tools.

The fabrication that I followed consists of increasing first a uniform proton exchange layer on the top of the substrates, so to weaken the crystal structure at the surface and enhance the subsequent etching rates. This allowed an increase by 6 times in the etching rate with respect to the ordinary material, and achieving ribs waveguides

with depths of several hundred of nanometers by simply employing a standard patterned photo-resist as etching mask. The PE top-layer not only allows to significantly enhancing the etching rates of $LiNbO_3$ in the non-masked region, but also to automatically achieve an index increase in the vertical direction, needed to confine light in both directions, hence achieving ribs waveguides.

The reactive ion etching process has proved a strongly reduce the roughness of the substrate (it passes from ~3 nm to ~1.4 nm all the samples). On the other hand the roughness of the sidewalls which is important for the losses of the final waveguides structures is higher than in the other areas.

The process yielded waveguides with approximately the same slope of the sidewalls (~60° in all cases) for the different types of materials undoped and MgO doped $LiNbO_3$.

These fabrication and roughness preliminary results suggest there is no preferential side for fabricating ridges waveguides when choosing the C-$LiNbO_3$, on the other hand, the etching rate, side walls angles and of low roughness of the bottom and the sides suggest that it is more convenient to fabricate ribs waveguides on the originally +Z side when choosing MgO-$LiNbO_3$.

4.9 References

[1]   H. Hu, A.P. Milenin, R.B. Wehrspohn, H. Hermann, W. Sohler, "Plasma etching of proton exchange lithium niobate", J. Vac. Sci.tchnol. A. vol. **24**, 1012 (2006).

[2]   Z. Ren, P.J. Heard, J.M. Marshall, P.A. Thomas, and S.Yu, "Etching characteristics of $LiNbO_3$ in reactive ion etching and inductively coupled plasma", J. Appl. Phys. **103**, 034109 (2008).

[3]   R.V. Schmidt and I.P. Kaminow, "Metaldiffused optical waveguides in $LiNbO_3$", Appl. Phys. Lett.**25**, 458 (1974).

[4]   W. S. Yang," Asymmetry ridge structure fabrication and reactive ion etching of $LiNbO_3$", Optical materials, **27**, 1642 (2005).

[5]   J.L. Jackel, C.E. Rice, J.J. Veselka, "proton exchange for high index waveguides in $LiNbO_3$", Appl. Phys. Lett, **41**, 607 (1982).

[6]   M. De Micheli, J. Botnieau, P. Sibillot and D.B. Ostrowsky, "Fabrication and characterization of titanium indifused proton exchange waveguides in Lithium niobate", Opt.Comm, **42**, 101(1982).

[7]   M.N. Armenise," fabrication techniques of the lithium niobate waveguides", IEE PRCEEDINGS,Vol.**125**, Pt. J, NO.2, APRIL(1988).

[8]   R. S. Weis, T.K. Gaylord, "Lithium niobate: summary of physical properties and crystal structure", Applied Phys, **37**, 191 (1985).

[9]   K.K. Wong, GEC.J.Res, **3**, 243 (1985).

[10]   Yu. N.Korkishko and V.A. Fedorov, "Ion exchange in single crystal for integrated optics and optoelectronics", Cambridge international science publishing, England (1999).

[11]   D.F. Clark, A.C.G Nutt, K.K. Wong, P.J.R. Laybourn, and R.M. De La Rue, "Characterization of proton exchange slab optical waveguides in z cut", J. Appl.Phys.**54**, 6218 (1983).

[12]   M.L. Bortz, "Quasi phase matched optical frequency conversion in lithium niobate waveguides", PhD. Dissertation, Department of Applied physics, Stanford University, Stanford, USA (1994).

[13]   Miroposit S1800 photoresist un-dyed series spin speed curves.

[14] Winfried Sabisch, and Matthias Kratzer, Ralf Peter Brinkmann," Energetic neutral flux towards surfaces in a magnetically enhanced reactive ion etch-like reactor", J. Vac. Sci. Technol. A **21**(4), 1205 (2003).

[15] Kouichi Ono, Mutumi Tuda, Hiroki Ootera, and Tatsuo Oomori, "Electron cyclotron resonance plasma etching of Si with Cl2: plasma chemistry and mechanisms", pure & Appl. Chem, Vol.**66**, 1327 (1994).

[16] Daniel. L. Flamm, "Mechanism of the silicon etching in fluorine and chlorinecontaining plasmas", Pure and Appl. Chem., Vol.**62**, No.9, 1709 (1990).

[17] H. Hui, R. Ricken and W. Sohler, "Etching of Lithium niobate: form Ridge waveguides to Photonic crystal structure", Eindhoven, The Netherlands, June 11-13-2008.

5. Conclusion, further work and future developments

5.1 Summary

The aim of this Master thesis was the fabrication of ridge waveguides in nonlinear crystals of the $LiNbO_3$ family by microstructuring techniques. The ridge structures used in this work would avoid the light spreading in the transverse dimension and keep all the light well confined. A layer of PE was created as the core guiding and confinement region on the Lithium niobate substrate.

Lithium niobate as reminded is an extensively studied material and there is still a huge amount of interest around the material and its applications. For its manifold properties, $LiNbO_3$ is one of the most widely used crystals to realize many devices employed in different field of science and technology. As matter of fact, $LiNbO_3$ is characterised by large pyroelectric, piezoelectric, nonlinear and electro-optic coefficients and it is also employed for applications in which acoustic and acousto-optic properties are necessary..

The MgO-doped Lithium Niobate combines the properties of the Congruent Lithium Niobate by also assuring a wider field of application by reducing the photorefration. In this master thesis both Congruent and MgO-doped Lithium Niobate were used.

Photolithography patterning techniques were used to coat the substrate surface with a resist film then patterned by exposure to UV light through a mask containing the desired ridge pattern. Ridges with depths of several hundred of nanometres height were then fabricated by reactive ion etching. A proper selectivity and a high resolution structuring of $LiNbO_3$ was achieved with a relatively simple photoresist mask, by optimizing the reactive ion etching of the substrate.

5.2 Further work

The further work that can be done on the waveguides implies their optical characterization concerning measurements of important parameters to determine the waveguide performance such as effective indices, cutoff wavelengths for the different propagation modes, insertion losses, modal intensity distributions and propagation loss, the latter being a particular important parameter to evaluate for the case of ridge wave-

guides (which can suffer from enhanced scattering losses due to roughness at the wall surfaces).

5.3 **Future developments**

Further developments could involve the integration of such structures with preexisting periodically poled ferroelectric gratings (PPLN) for high efficient frequency conversion in the visible and near infrared spectral regions [1].

Because of the ferroelectric properties of the $LiNbO_3$ crystal [2], by applying a high voltage electrical pulse along its optical axis one can achieve a reversal of the ferroelectric polarity through the crystal. Periodically Poled Lithium Niobate (PPLN) structures fabricated by electric field poling are suitable for the quasi phase matching of many nonlinear optical applications of practical interest, e.g. second harmonic generation (SHG), difference frequency generation (DFG), and optical parametric oscillation (OPO). In a broader perspective, domain engineered structures at micro and nano scale lengths can open many interesting research topics [5]. By combining of PPLN and waveguides structures, one can improve the conversion efficiencies compared to bulk, due to the high energy density over a long interaction length Furthermore by using MgO-$LiNbO_3$ substrates one could suppress the photorefractive effect in applications where blue or green light is generated [3] [4].

5.4 **References**

[1] Kiyohide Sakai, Yasuharu Koyata, and Yoshihito Hirano, "Blue light generation in ridge waveguide MgO:LiNbO$_3$ crystal pumped by a fiber Bragg grating stabilizer laser diode", Optics letters/ vol.**32**, No.16/ August 15 (2007).

[2] R. S. Weis, T.K. Gaylord, Applied Phys, "Lithium niobate: summary of physical properties and crystal structure", A **37**, 191 (1985).

[3] D.H. Jundt, M.C.C Kajiyama, D.Djukic, M. Falk, "Optical methods to characterize crystal composition of MgO doped lithium neonate", Journal of crystal growth, **312**, 1109 (2010).

[4] M. Iwai, T. Yoshino, S. Yamaguchi, and M. Imaeda, "High power blue generation from a periodically poled MgO-LiNbO$_3$ ridge type waveguide by frequency doubling of diode and pumped Nd:Y$_3$L$_5$O$_{12}$ laser", Applied physics letter, vol.**83**, 18 (2003).

[5] Sunao Kurimura, Yuji Kato, Masayuki Maruyama, Yusuke Usui, and Hirochika Nakajima, "Quasi phase matched adhered ridge waveguide in LiNbO$_3$", Applied physics letters, **89**, 191123 (2006).